MINERALOGICAL AND CHEMICAL COMPOSITION OF SHALE AT MULTIPLE SCALES

by

Joseph Douglas Levinthal

A thesis submitted to the faculty of
The University of Utah
in partial fulfillment of the requirements for the degree of

Master of Science

in

Nuclear Engineering

Department of Civil and Environmental Engineering

The University of Utah

August 2016

The University of Utah Graduate School

STATEMENT OF THESIS APPROVAL

The thesis of **Joseph Douglas Levinthal**

has been approved by the following supervisory committee members:

Luther W. McDonald IV	, Chair	**May 10, 2016** Date Approved
Terry Ring	, Member	**May 10, 2016** Date Approved
Michael Simpson	, Member	**May 10, 2016** Date Approved

and by **Michael Barber** , Chair/Dean of

the Department/College/School of **Civil and Environmental Engineering**

and by David B. Kieda, Dean of The Graduate School.

ABSTRACT

This work provides a better understanding of radionuclides associated with shale formations and an increase in their concentration accompanying oil and gas production. The mineralogical and inorganic composition of various hydrocarbon rich shales was evaluated with spectroscopic, microscopic, and mass spectrometric techniques. Microstructural analysis by X-ray Diffraction (XRD) determined the quartz, feldspar, dolomite, calcite, and clay composition of the shale. Scanning Electron Microscopy - Energy Dispersive X-ray Spectroscopy (SEM/EDX) revealed the presence of inorganic metals (i.e. U, Th, Pb, etc.) near hydrocarbon rich regions of the shale. Elemental analysis of the bulk mineral phases via multi-collector Inductively Coupled Plasma Mass Spectrometry (ICP-MS) revealed higher concentration of U and Th associated with the organics in shale. A combination of the geochemical and mineralogical data suggests that the anoxic conditions during deposition may have led to the enrichment of the redox-sensitive elements (i.e. U, V, and Mo, etc.) in the Utica and Niobrara formations, while an oxic depositional environment led to a depletion of redox-sensitive elements in the Green River and Mancos formations. Furthermore, our data suggest that rare-earth elements (REE) enrichment is of terrigenous origins, supporting anoxic diagenesis. Knowledge of the inorganic composition, including Naturally Occurring Radioactive Materials (NORM) and Technologically Enhanced Naturally Occurring Radioactive

Materials (TENORM) of hydrocarbon rich shales, is essential for the development of advanced environmental techniques that extract the hydrocarbons without polluting the surrounding environment.

TABLE OF CONTENTS

LIST OF FIGURES

LIST OF TABLES

ACKNOWLEDGEMENTS

I would like to express gratitude to my honorable supervisor Luther McDonald IV for his continuous guidance, support, scientific advice, and insights. I am very happy to work with him and grateful for his intensive care during my path to a masters degree.

I am also grateful to my committee members Terry Ring and Michael Simpson for their continued support, use of laboratory facilities, and assistance working through my thesis.

I must give special thanks to Mathew Snow and Matthew Watrous for continuous assistance and encouragement during my internship with Idaho National Laboratory.

I would also like to thank the faculty and staff at Idaho National Laboratory; I had a rewarding experience with them.

Finally, I want to remember my parents, classmates, and friends for their inspiration and suggestions to finish this work; we all did this together.

CHAPTER 1

INTRODUCTION

Concerns have escalated over the long-term sustainability of the current energy dependence on fossil fuels. These concerns have also been shaped by the risks of rising greenhouse gas emissions, and pollutants that are driving the global climate change (Werner et al., 2015). Many different technologies are competing to be a valid energy production alternative, or a compliment to fossil fuels. Unconventional gas production from shale formations is an option (Clarkson, 2013, Chermak et al., 2014, Wang et al., 2014). Shale gas can contribute to the self-sufficiency of a nation. The shale gas boom reduced US natural gas imports in 2011 to levels only previously seen in 1994 (Wang et al., 2014). Also, a substantial shift from coal to natural gas in power generation and lower oil use in the transport sector has led to a reduction in the US's carbon dioxide emission. Globally, there are many large unconventional reservoirs (encompassing mudstones or 'shale', tight sand, and carbonate) that could help alleviate some of the energy concerns, but sustainable and environmentally sound production of natural minerals, noble metals, and hydrocarbons (gas and/-or oil) from these shale formations has presented many challenges (Landa, 2004, Weijermars et al., 2011, Clarkson et al., 2012, Haque et al., 2014, McGlade et al., 2013). Naturally, accompanying the benefits of the shale gas

extraction are environmental concerns and the continual expansion of natural gas production; therefore, the environmental issues associated with the shale gas have become increasingly controversial. Of course, potential negative environmental impacts have negatively influenced public opinion, which is slowing and even halting the shale gas expansion (Wang et al., 2014). Challenges include environmental concerns of exploration and drilling, contamination of water resources with the use of proppant and associated hydraulic fracturing chemicals and/-or radioactive waste, wastewater management, and human exposure to radioactive nuclides (Bowell et al., 2011, Chermak et al., 2014, Rivard et al., 2014, Wang et al., 2014, Bhargava et al., 2015). Furthermore, the production of the technologically enhanced naturally occurring radioactive materials (TENORM) during hydraulic fracturing can create many challenges including increased cost of waste disposal and personnel exposure to radioactivity (Galindo et al., 2007, Sovacool, 2014). To mitigate these risks, one must first know the concentration of radionuclides contained in the shale and the viability of those radionuclides becoming solubilized. The concentration and morphological properties of the elements and minerals in shale was evaluated using microscopic, spectroscopic, and crystallographic techniques. This combination of techniques provides not only bulk determination of the mineral associations, but also microscopic views of the elemental association to the hydrocarbons of interest.

Shale is a fine-grained (modal grain size of <65 μm) and finely stratified sedimentary rock formed from consolidated muds (commonly dominated by clay minerals and subordinate silicate and carbonate minerals) and is the most abundant type of sedimentary rock (Swanson, 1961, Tribovillard, 2006, Tribovillard et al., 2008). Shales are composed

of sediments that formed from a variety of sources, including ancient ocean trenches to Himalayan lakes, and range in climates from Antarctica to tropical jungles (Swanson, 1961, Tribovillard, 2006, Tribovillard et al., 2008). This incredible range in depositional environments and sediment provenance is reflective of the wide variety of minerologies and fabrics (including tectonically induced textures) inherent to shales. One common denominator amongst shales is the potential for the development of hydrocarbons from organic matter as the result of deposition and geological evolution of shales within zones of anoxia in both marine and lacustrine environments. Consequently, this led to the notion that shales represented the source of hydrocarbons that then migrated into conventional sandstone reservoirs. More recently, these source-rock shales have become the focus of hydrocarbon production themselves due to much of the hydrocarbons (oil and/-or gas) still residing within these formations. Shale has also been found to be source rock for petroleum, natural gas, and many metals used in industry (Baj et al., 2013, Berlendis, 2014).

In this study, a wide variety of unconventional rock samples were studied using spectroscopic and microscopic techniques to determine the elemental composition and morphology of the constituents. Investigating the morphological properties of unconventional reservoir rocks builds a comprehensive story of the depositional environment of sediments and mineralogical associations, which leads to a more advanced understanding of the sedimentological evolution of the micro and macro environments, and is key to the reconstruction of basin, past oceans, landscapes, climates, and climate cycles. This knowledge and characterization of the unconventional reservoir samples will reduce waste and contamination during the extraction process. Continued

research will enhance the development of environmentally safe techniques for the extraction of fossil fuels and minerals.

The aim of Chapters 1 and 2 are to provide the theoretical background necessary for this thesis. Chapter 1 introduces shale's role in energy production, shale sedimentary makeup, and contamination concerns surrounding oil, gas, and mineral extraction. The three analytical methods used, Scanning Electron Microscopy with Energy Dispersive X-ray analysis (SEM – EDX), X-ray Diffraction (XRD), and Inductively Coupled Plasma Mass Spectrometry (ICP – MS), will be discussed throughout Chapter 2. XRD was used to determine the quartz, feldspar, dolomite, calcite, and clay composition of the shale. SEM/EDX provided insight into the inorganic metal composition near hydrocarbon rich regions of the shale. The elemental concentrations in the shale were quantified by complete dissolution of the shale using a microwave-acid digestion and analyzing the resulting solutions by multi-collector ICP – MS.

1.1 References

(1) Bai, Y.; Liu, Z.; Sun, P.; Liu, R.; Hu, X.; Zhao, H.; Xu, Y. Rare Earth and Major Element Geochemistry of Eocene Fine-Grained Sediments in Oil Shale- and Coal-Bearing Layers of the Meihe Basin, Northeast China. *J. Asian Earth Sci.* 2015, *97*, 89–101.

(2) Berlendis, S.; Beyssac, O.; Derenne, S.; Benzerara, K.; Anquetil, C.; Guillaumet, M.; Estève, I.; Capelle, B. Comparative Mineralogy, Organic Geochemistry and Microbial Diversity of the Autun Black Shale and Graissessac Coal (France). *Int. J. Coal Geol.* 2014, *132*, 147–157.

(3) Bhargava, S. K.; Ram, R.; Pownceby, M.; Grocott, S.; Ring, B.; Tardio, J.; Jones, L. A Review of Acid Leaching of Uraninite. *Hydrometallurgy* 2015, *151*, 10–24.

(4) Bowell, R. J.; Grogan, J.; Hutton-Ashkenny, M.; Brough, C.; Penman, K.; Sapsford, D. J. Geometallurgy of Uranium Deposits. *Miner. Eng.* 2011, *24*, 1305–1313.

(5) Chermak, J. a.; Schreiber, M. E. Mineralogy and Trace Element Geochemistry of Gas Shales in the United States: Environmental Implications. *Int. J. Coal Geol.* 2014, *126*, 32–44.

(6) Clarkson, C. R. Production Data Analysis of Unconventional Gas Wells: Review of Theory and Best Practices. *Int. J. Coal Geol.* 2013, *109-110*, 101–146.

(7) Galindo, C.; Mougin, L.; Nourreddine, A. An Improved Radiochemical Separation of Uranium and Thorium in Environmental Samples Involving Peroxide Fusion. *Appl Radiat Isot* 2007, *65*, 9–16.

(8) Haque, N.; Norgate, T. The Greenhouse Gas Footprint of in-Situ Leaching of Uranium, Gold and Copper in Australia. *J. Clean. Prod.* 2014, *84*, 382–390.

(9) Landa, E. R. Uranium Mill Tailings: Nuclear Waste and Natural Laboratory for Geochemical and Radioecological Investigations. *J. Environ. Radioact.* 2004, *77*, 1–27.

(10) McGlade, C.; Speirs, J.; Sorrell, S. Unconventional Gas – A Review of Regional and Global Resource Estimates. *Energy* 2013, *55*, 571–584.

(11) Rivard, C.; Lavoie, D.; Lefebvre, R.; Séjourné, S.; Lamontagne, C.; Duchesne, M. An Overview of Canadian Shale Gas Production and Environmental Concerns. *Int. J. Coal Geol.* 2014, *126*, 64–76.

(12) Skalak, K. J.; Engle, M. a.; Rowan, E. L.; Jolly, G. D.; Conko, K. M.; Benthem, A. J.; Kraemer, T. F. Surface Disposal of Produced Waters in Western and Southwestern Pennsylvania: Potential for Accumulation of Alkali-Earth Elements in Sediments. *Int. J. Coal Geol.* 2014, *126*, 162–170.

(13) Sovacool, B. K. Cornucopia or Curse? Reviewing the Costs and Benefits of Shale Gas Hydraulic Fracturing (fracking). *Renew. Sustain. Energy Rev.* 2014, *37*, 249–264.

(14) Swanson, V. E. Geology and Geochemistry of Uranium in Marine Black Shales: A Review. *USGS Prof. Pap.* 1961, *365*, 50pp.

(15) Tribovillard, N.; Algeo, T. J.; Lyons, T.; Riboulleau, A. Trace Metals as Paleoredox and Paleoproductivity Proxies: An Update. *Chem. Geol.* 2006, *232*, 12–32.

(16) Tribovillard, N.; Bout-Roumazeilles, V.; Algeo, T.; Lyons, T. W.; Sionneau, T.; Montero-Serrano, J. C.; Riboulleau, A.; Baudin, F. Paleodepositional Conditions in the Orca Basin as Inferred from Organic Matter and Trace Metal Contents. *Mar. Geol.* 2008, *254*, 62–72.

(17) Wang, Q.; Chen, X.; Jha, A. N.; Rogers, H. Natural Gas from Shale Formation – The Evolution, Evidences and Challenges of Shale Gas Revolution in United States. *Renew. Sustain. Energy Rev.* 2014, *30*, 1–28.

(18) Weijermars, R.; Drijkoningen, G.; Heimovaara, T. J.; Rudolph, E. S. J.; Weltje, G. J.; Wolf, K. H. a. a. Unconventional Gas Research Initiative for Clean Energy Transition in Europe. *J. Nat. Gas Sci. Eng.* 2011, *3*, 402–412.

CHAPTER 2

INSTRUMENTATION

2.1 Scanning Electron Microscope/ Energy Dispersive X-ray Spectroscopy

The scanning electron microscope (SEM) is used for the observation and characterization of heterogeneous organic and inorganic materials down to the nanometer scale. A scanning electron microscope (SEM) is a microscope that uses electrons instead of light to magnify objects. The major components of an SEM are the electron column, detectors, and the control console. The electron column is comprised of an electron gun and two or more lenses, used to influence the paths of electrons traveling through the evacuated tube (about 10^{-6} Torr) (Michael, 2003). Scanning electron microscopes are capable of high levels of magnification, great depth of field, and high resolution. They are often used to display morphological data, and are commonly used in tandem with EDX detectors to gather elemental composition on samples.

The micro-volume to be analyzed is irradiated with a finely focused electron beam. The beam is swept in a raster across the surface of the sample to form topographical images. A static beam can be used to obtain an analysis at one position. There are many different types of signals produced from the interaction of the electron beam with the sample and include: secondary electrons, backscattered electrons, characteristic x-rays,

and other photons at various energies. Many characteristics of the sample can be examined from these signals (i.e. surface topography, crystallography, composition, etc.). As a result of electron bombardment, characteristic x-rays are emitted. Analysis of the characteristic x-rays yields both qualitative identification and quantitative elemental information from a 1 μm diameter and 1 μm depth region on the sample (Hall, 1966).

2.1.1 Imaging Capabilities

SEM is one of the most versatile instruments used for the examination and analysis of the microstructural characteristics of solid objects. The SEM's usefulness stems from the high resolution of the images obtained when bulk objects are examined (Hall, 1966). The high-resolution micrographs shown in Figure 2.1 and Figure 2.2 were taken with a field emission gun SEM under routine operating conditions of the Utica formation shale sample taken at 39.0 feet from the Ohio Well. The image, Figure 2.1, is of bitumen (the dark area) surrounded by barite (bright areas) and other minerals. The large depth of field of the scanning electron microscope, the shadow relief effect of the secondary and backscattered electron contrast creates the appearance of the three-dimensional images (Michael, 2003). The high-resolution image in Figure 2.2 is of planktonic foraminifera, highlighting the details and size of the porous skeleton. Fossil foraminifera are useful in biostratigraphy, paleoecology, paleobiogeography, and oil exploration (Michael, 2003).

2.1.2 Elemental Analysis

Characteristic x-rays can be used to obtain compositional information from a sample. An electron probe microanalyzer (EPMA) coupled with an energy-dispersive

spectrometer (EDS) are the instruments used for obtaining localized chemical analysis of solid samples. The EDS system is used to evaluate the elemental makeup of samples along with rapid qualitative, and accurate quantitative, analysis. The electron beam interacts with the tightly bound inner shell electron of the sample atom, ejecting an electron from the shell. The atom is left in an excited energetic state with a missing inner shell electron. The inner shell vacancy is filled through a limited set of electron transitions from an outer shell. There are two ways an atom can release excess energy, through the Auger process and the emission of an x-ray photon. In the Auger process, the difference in shell energies is transmitted to another outer shell electron, ejecting it from the atom as an electron with a specific energy (Hall, 1966, Michael, 2003). The sharply defined energy of the characteristic x-ray arises from energy difference in between electron shells. Moseley's law is used for identification of elemental constituents. The energy difference between shells changes in a regular step fashion with the change in atomic number and is expressed by the following equation:

$$E = A(Z - C^2) \qquad 2.1$$

where E is the energy of the x-ray line, A and C are constants related to each x-ray series (Hall, 1966, Michael, 2003).

Figure 2.3 is a sub-sample from the Utica formation and prepared as polished thin section embedded in an epoxy 'puke' and carbon coated, using the method of Gottlieb et al. (2000) and Pirrie et al. (2004), which illustrates the capability of compositional mapping of the SEM coupled with EDS. Figure 2.3 shows the distribution of C, Mg, Al,

Si, S, K, Ca, Ti, Cr, Mn, Fe, Co, Mo, Pb, U in the shale sample.

2.2 X-Ray Diffraction

Presented here is a basic discussion on the principles of x-ray powder diffraction (XRD). X-rays are electromagnetic waves on the order of 1 angstrom ($1x10^{-10}$ m) and are used to understand the geometry of x-ray diffraction from crystals; this understanding creates a useful analysis of sample crystallography (Dinnebier, 2008). Classical electromagnetic waves are described by a sine wave that repeats periodically every 2π radians. The wavelength, λ, is the spatial length of each period. When two identical waves are not coincident, the waves have a "phase shift" with respect to each other, measured in two ways, as a linear shift, Δ, on a length scale, or as a phase shift, $\delta\phi$, on an angular scale, represented as:

$$\frac{\Delta}{\lambda} = \frac{\delta\phi}{2\pi} \Longrightarrow \delta\phi = \frac{2\pi}{\lambda}\Delta \qquad 2.2$$

XRD uses the measurement of the intensity of x-rays scattered from electrons bound to atoms (Dinnebier, 2008). X-rays scattered from atoms at different positions arrive at the detector with a relative phase shift. The measured intensities give information about the relative atomic positions. The detected intensities, I, is the square of the amplitude, A, of the sine wave. When two or more waves are present, the resulting amplitude depends on the phase shift $\delta\phi$. Two cases arise: $\delta\phi=0$, known as constructive interference, where $I=(A_1+A_2)^2$, and $\delta\phi=\pi$, destructive interference, where $I=(A_1-A_2)^2$. When more than two waves are present, intensity is represented by Equation 2.3 (Dinnebier, 2008).

$$I = \left[\sum_j A_j \exp(i\phi_j)\right]^2 \quad 2.3$$

where the sum is over all the sine waves present and the phases, ϕ_j, are measured with respect to some origin.

The far-field Fraunhofer approximation is used to simplify the mathematics to calculate the detected intensities. The incident x-rays scattered by single electrons are outgoing spherical waves that appear as plane waves in the far field, allowing for the use of Equation 2.3 to represent the intensity of the diffracted x-rays. The phases, ϕ_j, from Equation 2.3 and the measured intensity, I, is dependent on the atoms position, j, and the directions of the incoming plane waves and the scattered plane waves. The wave-vectors of the incoming and scattered waves are known, which leads to the relative atomic positions from the detected intensities. Diffraction occurs because the x-rays are on the order of separation of the atoms in a crystalline lattice, which gives rise to the powder diffraction pattern through a procedure created by Debye and Scherrer in 1916 (Dinnebier, 2008).

The Bragg equation (W. L. Bragg, 1912) is used to access the structural information in powder diffraction. The Bragg equation describes the principle of x-ray diffraction in terms of a reflection of x-rays by sets of lattice planes, which are crystallographic planes characterized by the Miller indices, *hkl*. The crystallographic planes are parallel and separated by a distance, d_{hkl}. Constructive interference only occurs when Bragg's law is satisfied for parallel planes of atoms, separated by a distance d_{hkl}.

X-rays are able to penetrate deep into a material where additional reflections, all in the

same direction, occur at thousands of consecutive parallel planes. Since all x-rays are reflected in the same direction, superposition of the scattered rays occurs. Shown in Figure 2.5, the second wave travels a longer distance PN before and NQ after reflection occurs. Constructive interference only occurs when (Δ, path difference) Δ= PN+NQ is a multiple *n=0, ±1, ±2, ±3...* of the wavelength λ:

$$\Delta = n\lambda \tag{2.4}$$

All other cases produce destructive interference; this produces sharp intensity maxima that emerge from the sample at angles where Equation 2.4 is valid. At angles where Equation 2.4 is not valid, no intensity emerges. Figure 2.5 shows geometrically:

$$\Delta = 2d \sin\theta \tag{2.5}$$

where *d* represents the interplanar spacing of the parallel crystallographic planes and 2θ is the diffraction angle— the angle between incoming and outgoing x-rays (Dinnebier, 2008). Combining Equations 2.4 and 2.5 to obtain the Bragg equation yields:

$$n\lambda = 2d \sin\theta \tag{2.6}$$

X-rays are produced in a sealed-tube source that contains a cooper block with a metal target (anode), and a tungsten filament (cathode) with a high voltage difference between them. The tungsten filament is heated producing electrons and the large potential

difference between the cathode and the anode accelerates electrons at the metal target. The produced electrons create a cascade of electronic transitions within the target material. The target material's atoms emit electromagnetic radiation as they return to the ground state. The x-rays exit the vacuum tube through beryllium windows. Anode materials must be good conductors of heat and electricity, as well as having a high melting point. The most common target elements are Cu and Mo, with many others used for special applications (e.g. Cr, Fe, Co, Ag, and W). The Panalytical Xpert3 uses a Cu anode producing $K_{\alpha 1}$ - 1.54060, $K_{\alpha 2}$ – 1.54443, and K_{β} -1.39225 angstroms. The loss of energy of the electrons by the collisions with atoms takes place over multiple events, producing a continuous spectrum of x-rays referred to as white radiation. The maximum energy loss, E, relates to the shortest wavelength, λ, according to the equation:

$$E = eV = \frac{hc}{\lambda} \qquad 2.7$$

where e is the charge of an electron, V is accelerating voltage, h is Plank's constant, and c is the speed of light. Therefore, the higher the accelerating voltage of the x-ray generator, the shorter the required minimum x-ray wavelength, λ (Dinnebier, 2008). Characteristic radiation is produced when the energy of the accelerated electron is higher than the threshold value of the anode. This produces discrete peaks superimposed over the white radiation. The energy and wavelength of the peaks depends solely on the metal used for the anode and is due to the ejection of the electron from one of the inner electron shells. An electron from a higher atomic level fills the vacancy of the ejected electron followed by the emission of an x-ray photon characterized by the difference in energy between the

two atomic levels. Copper produces $K_{\alpha 1}$ – 1.54060, $K_{\alpha 2}$ – 1.54443, and K_{β} -1.39225 Å characteristic lines. The $K_{\alpha 1}$ and $K_{\alpha 2}$ lines originate from the splitting of the 2p orbitals. The K_{β} line arises from the transition of an electron from the 3p shell in the copper atom. Powder diffraction work often uses a Cu vacuum tube because it has the shortest wavelength above one Å, and good thermal conductivity, which allows for relatively high power to be applied (Klug et al., 1974, Percharsky and Zavalij, 2003, Dinnebier, 2008).

Optical elements are placed in the x-ray beam path to tailor the characteristics of the beam. A Ni filter is used to reduce the K_{β} radiation contamination from the Cu anode. The energy of the Cu K_{β} x-rays (λ=1.392 Å) is just slightly above the threshold energy of the Ni K absorption edge (λ=1.488 Å), and therefore absorbs the K_{β} strongly; on the other hand, K_{α} x-rays (λ=1.542 Å) energy is insufficient to excite this particular transition and is not readily absorbed (Klug et al., 1974, Percharsky and Zavalij, 2003, Dinnebier, 2008).

A scintillation counter point detector is used in the Panalytical Xpert3. X-ray photons interact with the thallium doped sodium iodide crystal, which emits photons in the blue region of the visible spectrum. The photons are converted to voltage pulses through the use of a photomultiplier tube. The number of electrons ejected by the photocathode is proportional to the number of visible photons that hit the scintillator, and this is proportional to the energy of the original x-ray photon (Klug et al., 1974, Percharsky and Zavalij, 2003, Dinnebier, 2008).

One of the most commonly used reflection geometries for flat-plate powder diffraction is the "Bragg-Brentano" geometry shown in Figure 2.6. The dotted-circle centered on the sample position represents the goniometer circle on which the image of the divergent

source of x-rays is focused by diffraction from the flat-plate powdered sample. The footprint of the beam on the sample is proportional to cos (θ) and may overflow the sample at very low scattering angles. Slits are used to control divergence of the incident and diffracted beam. The setup allows for the source and the detector to be swept through a set of angles (Klug et al., 1974, Percharsky and Zavalij, 2003, Dinnebier, 2008).

2.3 Inductively Coupled Plasma Mass Spectrometry

J.J. Thomson reported the m/z ratio of an electron to be 5.69×10^{-9} grams/coulomb on April 30, 1897 at the Royal Institution meeting, and began the history of mass spectrometry. After that meeting he said:

At first there were very few who believed in the existence of these bodies smaller than atoms. I was even told long afterwards by a distinguished physicist who had been present at my lecture at the Royal Institution that he thought I had been 'pulling their legs'

He went on to construct the first mass spectrometer for the determination of the mass to charge ratio of ions. In 1906, J.J. Thomson received the Nobel Prize in Physics "*in recognition of the great merits of his theoretical and experimental investigations on the conduction of electricity by gases".* After this time, mass spectrometry (MS) begins to play an important role in the sciences. Using MS for precision measurements of isotopic ratios allowed for the investigation of paleotemperatures, age determination of rocks, and the investigations of meteorites for nuclear astrophysics. One notable large-scale application was the Calutron separators used for the isotopic separation of the highly fissile ^{235}U needed for the Manhattan Project (Thomson, 1897, Münzenberg, 2013).

Research and improvements to all areas of mass spectrometry continue to this day,

with one focus being sample introduction. For example, inductively coupled plasma was initially invented as an ionization source for atomic emission spectrometry. Then, in 1970, Knewstubb and Hayhurst considered the high-temperature plasma as a means for an ion source for subsequent analysis by a quadrupole mass analyzer (Knewstubb and Reid, 1970). Feasibility studies started in 1971 at the University of Liverpool, with the first report made in 1974 at the Society of Analytical Chemistry (Gray and Tomlinson, 1974, Houk et al., 1974). Houk produced the first mass spectrum in 1978 at the Ames Laboratory after overcoming many difficulties (Jiang and Houk, 1987). The main difficulty was interfacing the ICP, which was operated at ambient pressure to a mass separator operated at a high vacuum. Once good spectra with high sensitivity could be demonstrated, then using the ICP as an elemental source made instrument development rapid.

ICP – MS has become an extremely powerful tool for elemental analysis, and has been used extensively for a vast range of samples including geological, environmental, and biological (Münzenberg, 2013). ICP – MS has the advantages of a large dynamic range and high sensitivity, making it ideal for quantitative analysis. It is also capable of isotopic determinations of many elements, making it a very useful tool for many applications.

The basic components that make up an ICP – MS system are shown in Figure 2.7. The liquid sample is introduced to a nebulizer with a peristaltic pump, where it is converted into a fine aerosol with argon gas. The fine droplets of the aerosol, which represent only 1–2% of the sample, are separated from larger droplets by means of a spray chamber. The fine aerosol emerges from the exit tube of the spray chamber and is

transported into the plasma torch through a sample injector, all shown in Figure 2.7A (Thomas, 1989, Thermo Fisher, 2012).

The plasma is formed by the interaction of an intense magnetically induced field, which is produced by radiofrequency (RF) passing through a copper coil, on a tangential flow of argon gas flowing through two concentric quartz tubes (torch). This gas is ionized and, when seeded with a source of electrons from a high-voltage spark, forms a very-high-temperature plasma discharge (~10,000 K) at the open end of the tube. In ICP – MS, the horizontally positioned plasma torch is used to generate positively charged ions, not photons. Photons are filtered prior to reaching the detector because they have the potential to increase signal noise. The production and the detection of large quantities of ions give ICP – MS its characteristic low parts-per-trillion (ppt) detection capability (Thomas, 1989, Thermo Fisher, 2012).

Once the ions are produced in the plasma, they are directed into the mass spectrometer via the interface region, which is maintained at a vacuum of 1–2 Torr with a mechanical roughing pump. This interface region in Figure 2.7B consists of a sampler and skimmer nickel cones, and an extraction lens, each with a small orifice to allow the ions to pass through to the ion optics, where they are guided into the mass separation device. The sample cone introduces ions from the plasma into the first vacuum stage (interface vacuum) and the skimmer cone admits the ions into the mass spectrometer. The extraction lens focuses and accelerates the ions from the back of the skimmer cone into the intermediate vacuum region of the analyzer (Thomas, 1989, Thermo Fisher, 2012).

The interface region is one of the most critical areas of an ICP mass spectrometer because the ions must be transported efficiently and with electrical integrity from the

plasma, which is at atmospheric pressure (760 Torr) to the mass spectrometer analyzer region at approximately 10^{-6} Torr (Thomas, 1989, Thermo Fisher, 2012).

Unfortunately, there is capacitive coupling between the RF coil and the plasma, producing a potential difference of a few hundred volts. If this were not eliminated, it would have resulted in an electrical discharge (called a secondary discharge or pinch effect) between the plasma and the sampler cone. Steps must be taken to ground the RF coil and eliminate the secondary charge. Once the ions have been successfully extracted from the interface region, they are directed into the main vacuum chamber by a series of electrostatic lens, or ion optics. Right angle positive ion deflection (RAPID) lens, collision cell (QCell), and the differential aperture (DA) plate make up the ion optics and are shown in Figure 2.7C. The RAPID lens lets the neutral particle from the plasma pass directly through the lens without interacting. Upon leaving the deflection device, the ions are focused onto the entry of the collision cell (QCell). It consists of a quadrupole with flat rods in a partially contained region and can be pressurized with helium gas to remove undesirable ions. From the QCell, the ion beam is focused onto a small differential aperture (DA plate), which separates the intermediate vacuum stage from the high vacuum analyzer region. Directly behind the DA plate, the beam is deflected again by the DA lens, which removes residual gas particles. The operating vacuum in this region is maintained at about 10^{-3} Torr. Figure 2.7D shows where the ions are then introduced into the quadrupole mass analyzer, which filters out ions of a specific mass to charge ratio, depending on the RF voltage and DC voltage applied to the quadrupole rods. Ions transmitted through the quadrupole are finally transferred to the dual mode secondary electron multiplier and detected. The final process is to convert the ions into an electrical

signal with an ion detector. This electronic signal is then processed by the data handling system in the conventional way and then converted into analyte concentration using ICP – MS calibration standards (Thomas, 1989, Thermo Fisher, 2012).

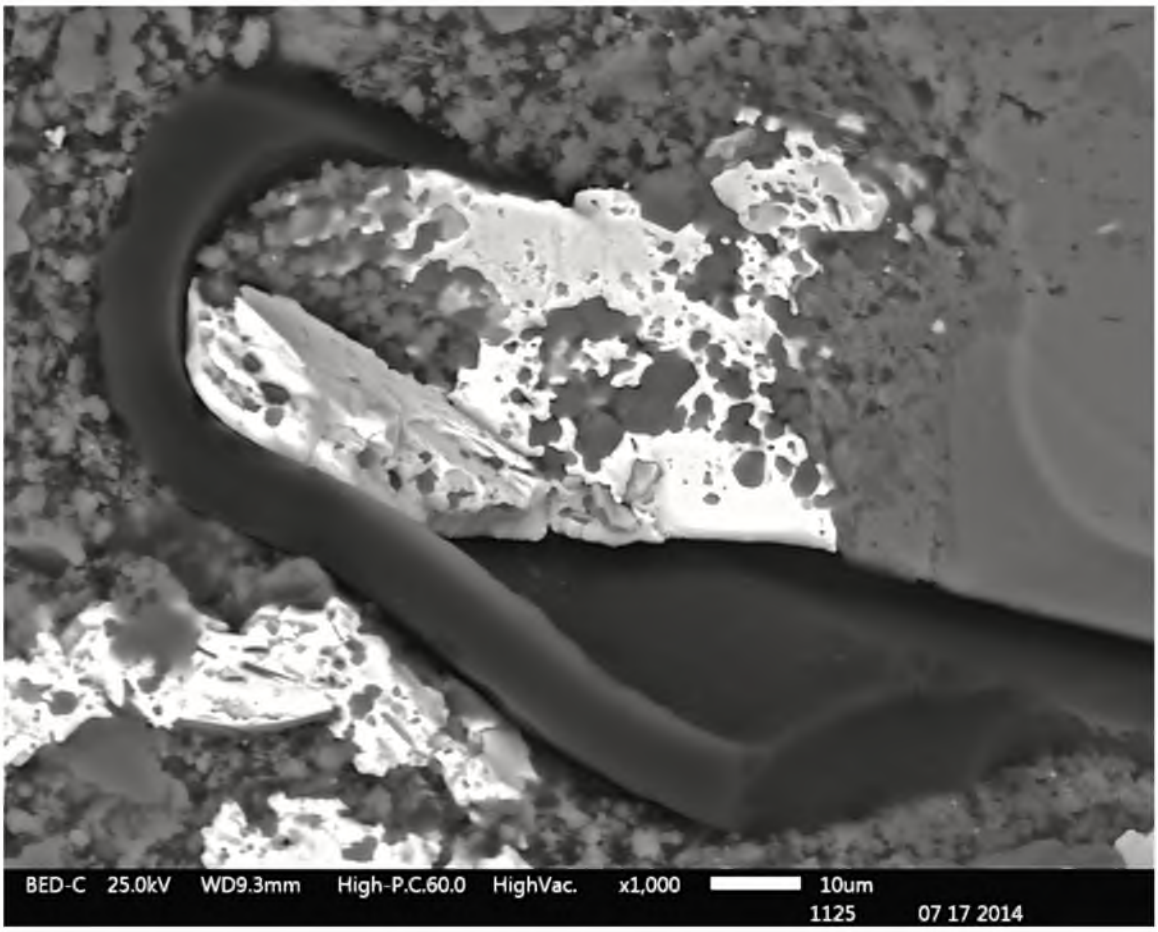

Figure 2.1 Bitumen and Barite SEM Image**.** Image shows Bitumen shown by the darkest areas and surrounded by barite shown in the bright areas, which are surrounded by other minerals. This figure also highlights the ability of SEM to produce three-dimensional-like images.

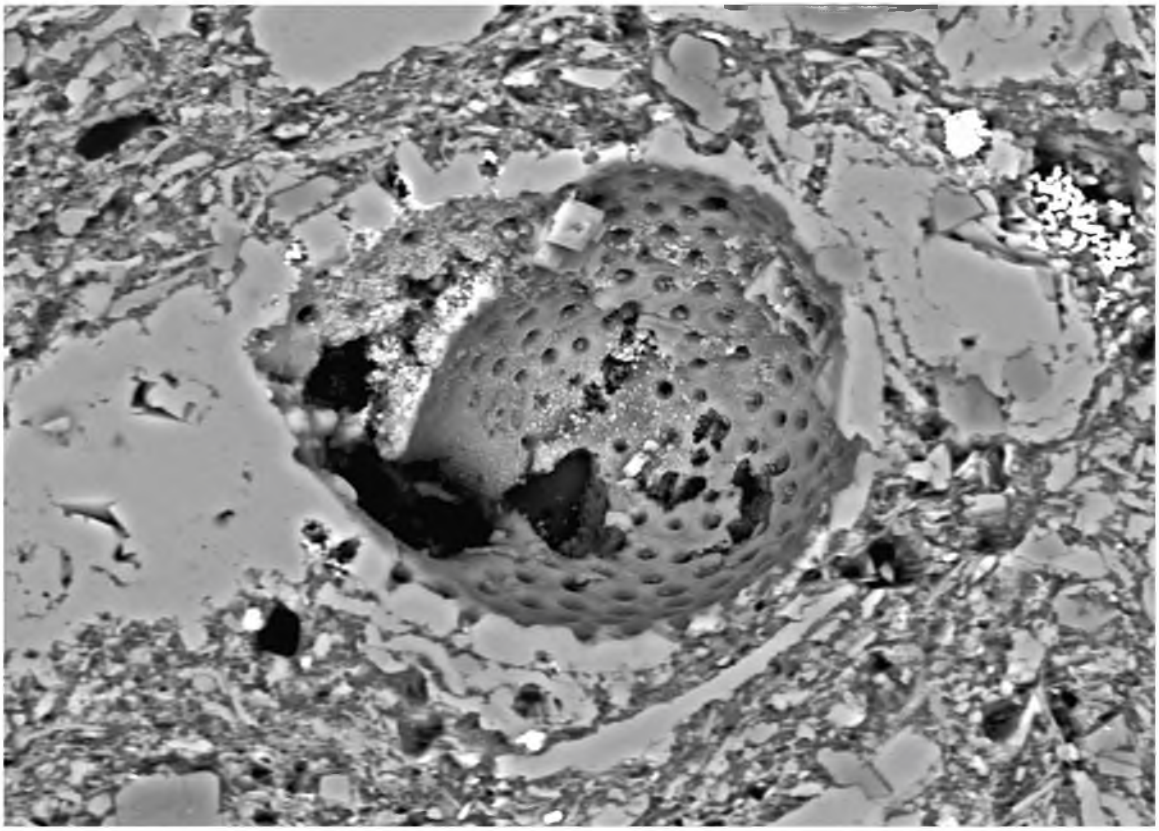

Figure 2.2 Planktonic Foraminifera**.** Sub-sample from the Utica formation of planktonic foraminifera, highlighting the details and size of the porous skeleton.

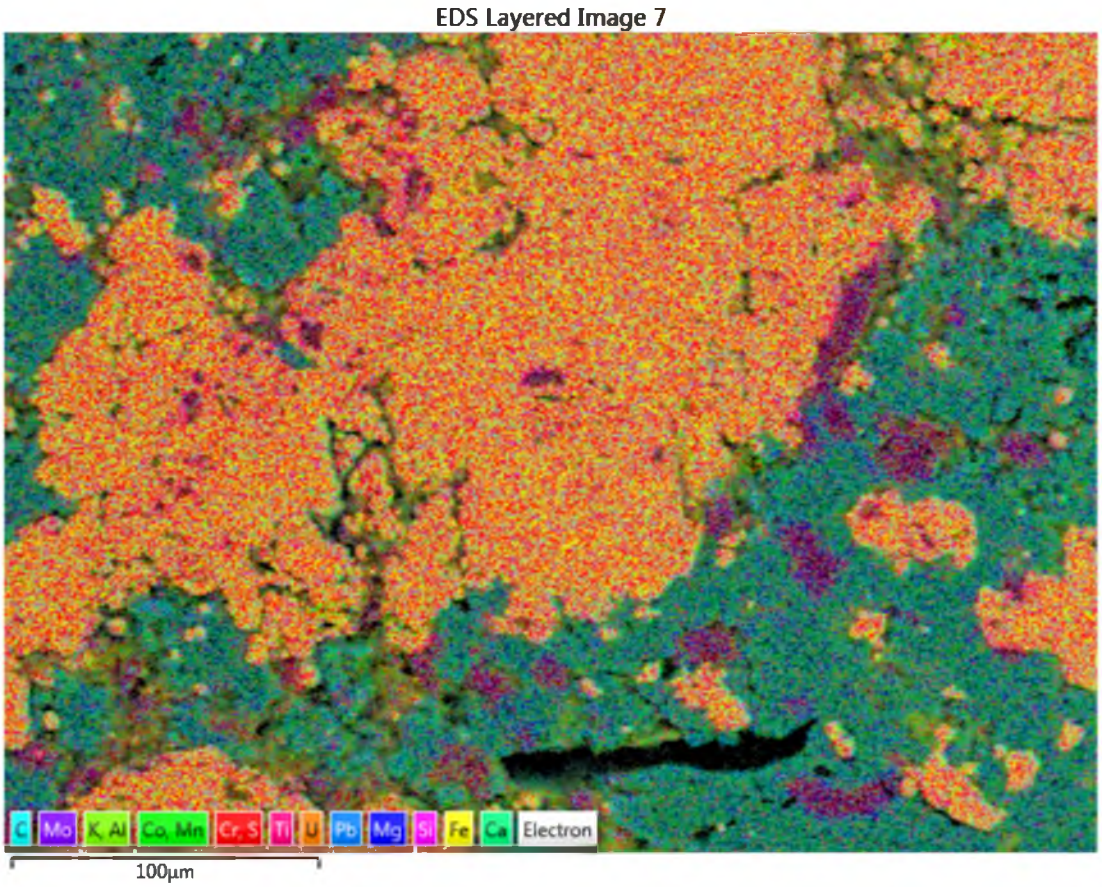

Figure 2.3 SEM Coupled with EDS. Sub-sample of the Utica formation, which lustrates the capability of compositional mapping of the SEM coupled with EDS. This figure shows the distribution of C, Mg, Al, Si, S, K, Ca, Ti, Cr, Mn, Fe, Co, Mo, Pb, U in the shale sample.

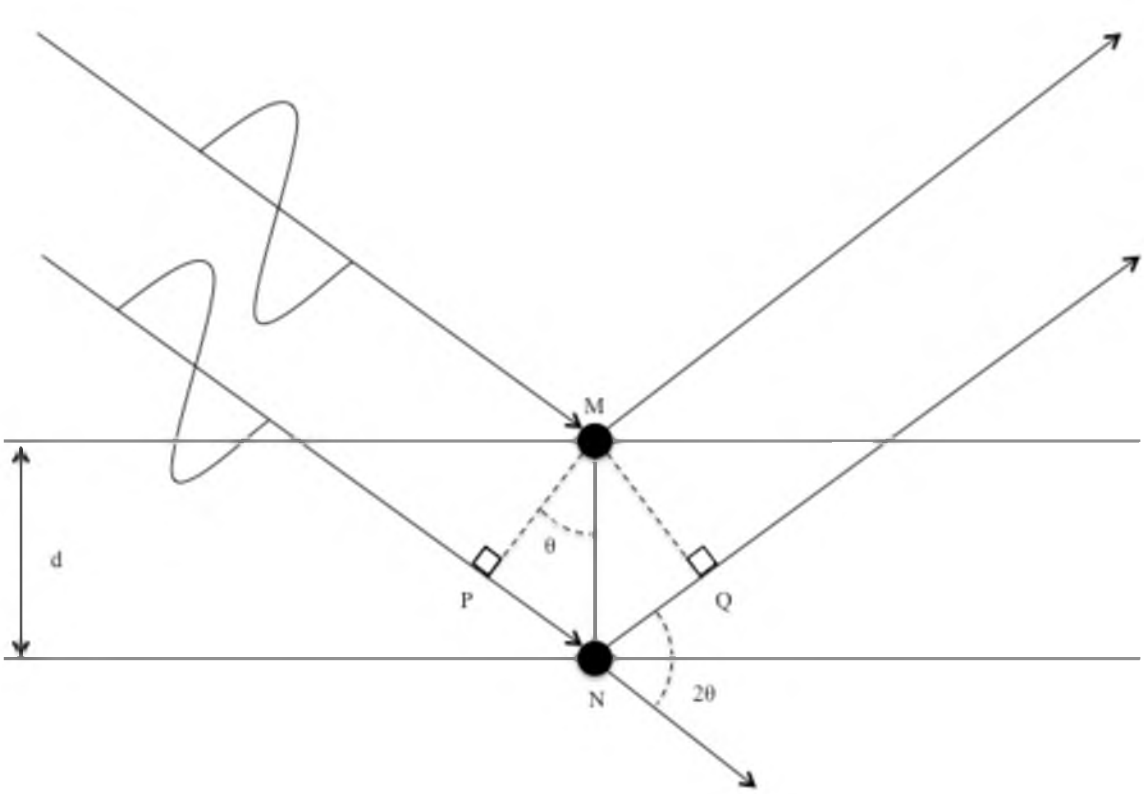

Figure 2.4 Bragg's Law Geometry. Illustration of the geometry used for the simplified derivation of Bragg's Law.

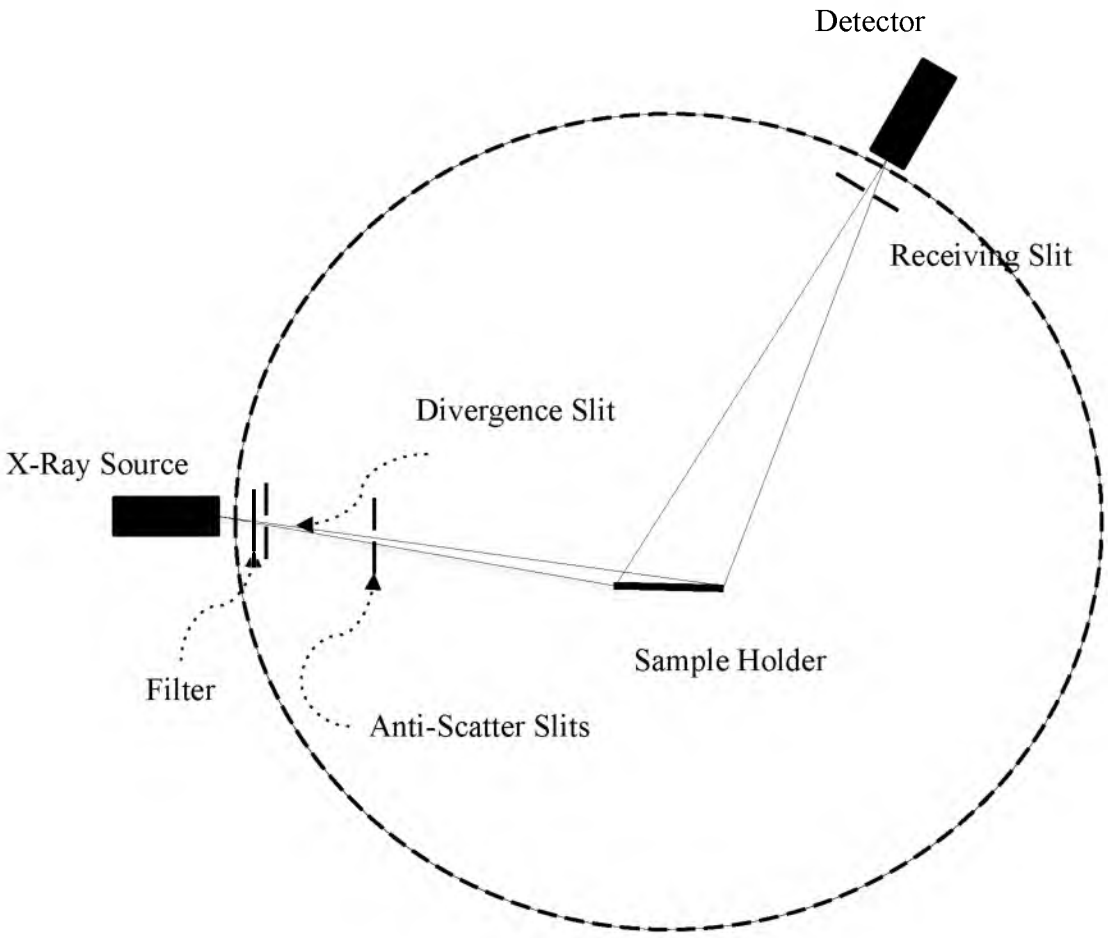

Figure 2.5 Bragg-Benot Geometry. Representation of the Bragg-Bento geometry. The dotted-circle centered on the sample position represents the goniometer circle on which the image of the divergent source of x-rays is focused by diffraction from the flat-plate powdered sample. Both the source and the detector are rotated about the axis.

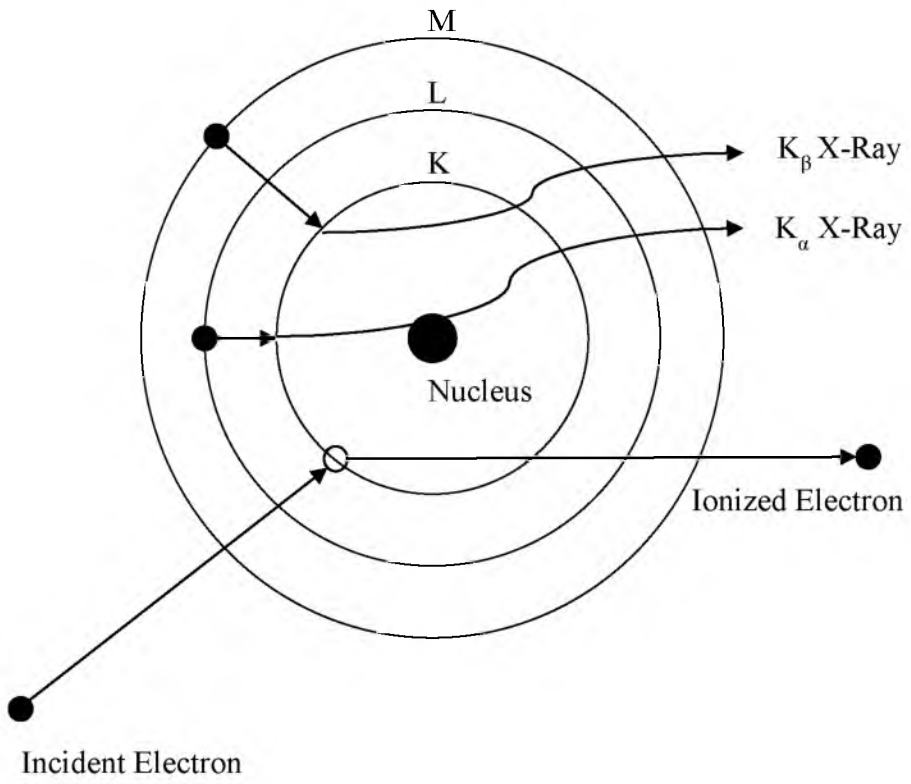

Figure 2.6 Energy Level Diagram. Energy level diagram representing electron excitations and emissions. K, L and M energy levels are indicated along with K_α and K_β emissions.

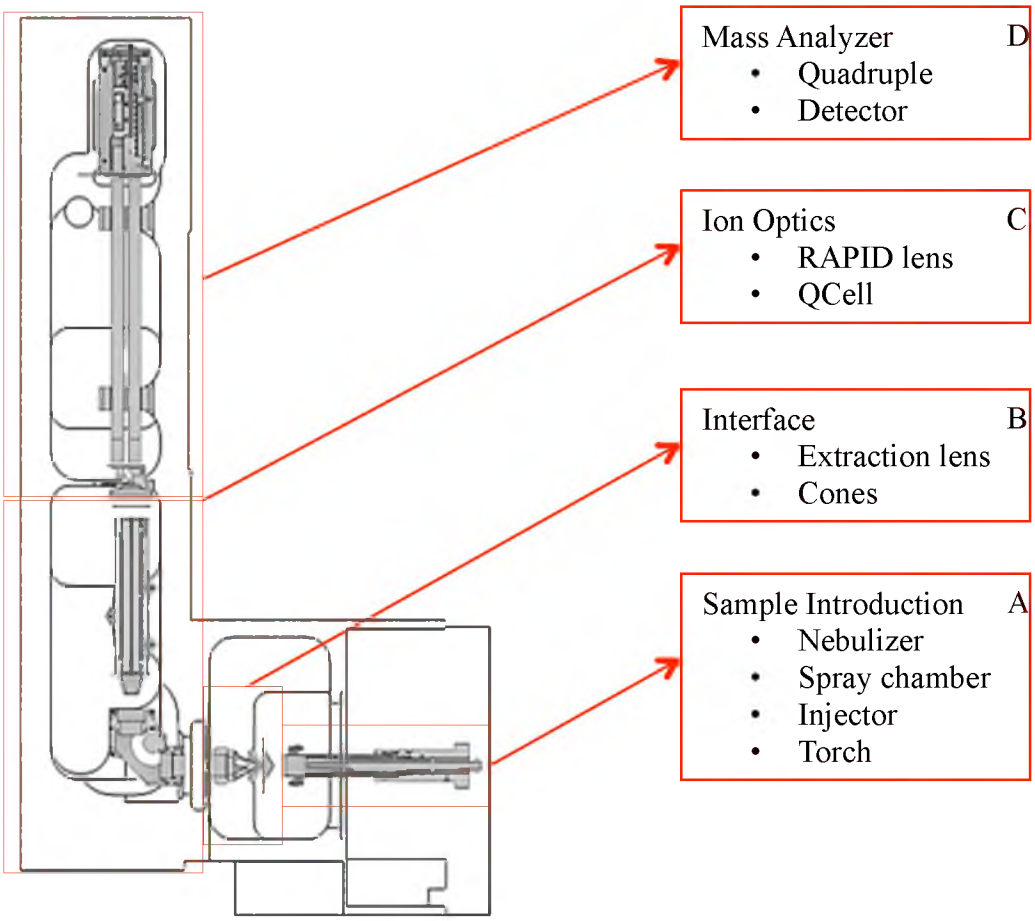

Figure 2.7 iCAP Q Schematic. iCAP Q (Thermo Scientific) instrument schematics-Front view. A) Sample introduction, B) Interface, C) Ion optics, D) Mass analyzer.

2.4 References

(1) Dinnebier, R. E. *Powder Diffraction Theory and Practivce*; 2008.

(2) Fisher, T. *iCAP Q Operating Manual*; 2012.

(3) Gottlieb; Wilkie; Sutherland; Suthers; Perera; Jenkins; Spencer; Butcher; Rayner. Using Quantitative Electron Microscopy for Process Mineralogy Applications. *J. Miner.* 200AD, *52*, 24–25.

(4) Gray; Tomlinson. Production of Short-Lived Molecules in a Mass Spectrometer. *Int. J. Mass Spectrom. Ion Phys.* 1974, *15*, 121–131.

(5) Hall, C. E. *Introduction to Electron Microscopy*; McGraw-Hill: New York, 1966.

(6) Houk, K. N.; George, J. K.; Duke, R. E. A Frontier Molecular Orbital Treatment of Fulvene Cycloadditions. Molecular Orbital Calculations and Photoelectron Spectra of Substituted Fulvenes. *Tetrahedron* 1974, *30*, 523–533.

(7) Jiang, S.-J.; Houk, R. S. Elemental and Isotopic Analysis of Powders by Inductively Coupled Plasma Mass Spectrometry with Arc Nebulization. *Spectrochim. Acta, Part B* 1987, *42*, 93–96.

(8) Klug, H. P.; Alexander, L. E. *X-Ray Diffraction Procedures*; 2nd ed.; John Wiley & Sons: New York, 1974.

(9) Knewstubb, P. F.; Reid, N. W. The Unimolecular Decomposition of Excited Polyatomic Ions Studied by Time of Flight Mass Spectrometry. *Int. J. Mass Spectrom. Ion Phys.* 1970, *5*, 361–380.

(10) Menzenberg, G. Development of Mass Spectrometers from Thomson and Aston to Present. *Int. J. Mass Spectrom.* 2013, *349-350*, 9–18.

(11) Michael, J. *Scanning Electron Microscopy and X-Ray Microanalysis*; 2003.

(12) Pecharsky, V. K.; Zavalij, P. Y. *Fundamentals of Powder Diffraction and Structural Characterization of Materials*; Kluwer Academic Publishers: Boston, 2003.

(13) Pirrie; Butcher; Power; Gottlieb; Miller. Rapid Quantitative Mineral and Phase Analysis Using Automated Scanning Electron Microscopy (QemSCAN); Potential Applications on Forensic Geosciences. In: Forensic Geoscience: Principles, Techniques and Application. *Geol. Soc.* 2004, *232*, 123–136.

(14) Thomas, R. *Practical Guide to ICP-MS*; 1989; Vol. 53.

(15) Thomson, J. J. Cathode Rays. *Journal of Science* 1897, *44*.

CHAPTER 3

MINERALOGICAL AND CHEMICAL COMPOSITION OF SHALE AT MULTIPLE SCALES

3.1 Abstract

This work provides a better understanding of radionuclides associated with shale formations and an increase in their concentration accompanying oil and gas production. The mineralogical and inorganic composition of various hydrocarbon rich shales was evaluated with spectroscopic, microscopic, and mass spectrometric techniques. Microstructural analysis by x-ray diffraction (XRD) determined the quartz, feldspar, dolomite, calcite, and clay composition of the shale. Scanning electron microscopy - energy dispersive x-ray spectroscopy (SEM/EDX) revealed the presence of inorganic metals (i.e. U, Th, Pb, etc.) near hydrocarbon rich regions of the shale. Elemental analysis of the bulk mineral phases via multi-collector inductively coupled plasma mass spectrometry (ICP-MS) revealed higher concentration of U and Th associated with the organics in shale. A combination of the geochemical and mineralogical data suggests that the anoxic conditions during deposition may have led to the enrichment of the redox-sensitive elements (i.e. U, V, and Mo, etc.) in the Utica and Niobrara formations, while an oxic depositional environment led to a depletion of redox-sensitive elements in the

Green River and Mancos formations. Furthermore, our data suggest that rare-earth elements (REE) enrichment is of terrigenous origins, supporting anoxic diagenesis. Knowledge of the inorganic composition, including Naturally Occurring Radioactive Materials (NORM) and Technologically Enhanced Naturally Occurring Radioactive Materials (TENORM) of hydrocarbon rich shales, is essential for the development of advanced environmental techniques that extract the hydrocarbons without polluting the surrounding environment.

3.2 Introduction

Unconventional shale reservoirs are being evaluated for their potentially large hydrocarbon (oil and/-or gas) reserves (Badics and Veto, 2012, Bernard et al., 2012, Sachsenhofer et al., 2012, Selley, 2012, Chermak et al., 2014). Many of these shale reservoirs have become prospectus due to recent advances in geological knowledge (i.e. that tight rocks are not only the source of hydrocarbons, but also a reservoir) and technology (i.e. hydraulic fracturing and recovery methods). Furthermore, shale reservoirs have grown in importance as a complement to conventional fossil fuels due to the increase in the world's energy demands (Weijermars et al., 2011). Many different technologies are competing to be a valid energy production alternative or compliment to fossil fuels and unconventional gas production from shale formations represents one option currently under consideration (Clarkson, 2013, Chermak et al, 2014,).

Globally, there are many large shale reservoirs that could help alleviate some of the current and predicted future energy demands, but sustainable and environmentally sound production of natural minerals, and hydrocarbons (gas and/-or oil) from these shale

formations has presented many challenges (Landa, 2004, Weijermars et al., 2011, Clarkson et al., 2012, McGlade et al., 2013, Haque and Norgate, 2014). Furthermore, the production of TENORMs during hydraulic fracturing of these shale reservoirs can create many challenges including increased cost of waste disposal and personnel exposure to radioactivity, mainly from ^{238}U, ^{232}Th, and their prodigy (Galindo et al., 2007, Sovacool, 2014, Skalak et al., 2014). To mitigate these risks and address other potential impacts, information about the shale, including mineralogy and element geochemistry, is critical (Chermak et al., 2014).

Shale is a fine-grained (modal grain size of <65 μm) and finely stratified sedimentary rock formed from consolidated muds, commonly dominated by clay minerals and subordinates silicate and carbonate minerals (Tribovillard et al., 2006). It is the most abundant of the sedimentary rocks being composed of sediments that formed from a variety of sources ranging from ancient ocean trenches to Himalayan lakes, and a range of climates from Antarctica to tropical jungles (Swanson, 1961). This incredible range in depositional environments and sediment provenance is reflective of the wide variety of minerologies and fabrics (including tectonically induced textures) inherent to shales.

Shale makes up to about three-fourths of all sedimentary rock and underlies more of the Earth's land surface than any other rock. Geochemical significance of shale arises from the organic rich nature. Additionally, the small particle size allows many colloidal processes to operate, which, along with the ion-exchange capacity of most clay minerals, make the composition of clays generally responsive to changes in setting that take place during sedimentation and diagenesis. During sedimentation and diagenesis in marine waters, the general trend of these changes is thought to result in clay-rich rocks

containing larger quantities of metallic elements compared to other rock types. Metals concentrated in shale by sedimentation and diagenesis may be source materials for ore deposits after the shale is metamorphosed, and understanding the way these metals are distributed in a large body of shale may lead to better search for such ore deposits. Similarly, the higher concentration of clays and kerogen could possibly lead to higher amounts of oil/and-or gas. The metals in shale may be released into the environment during weathering, erosion, or exploration.

Organic matter in sedimentary rocks derives mainly from phytoplankton and, to a lesser extent, zooplankton and bacteria, and thus also can be regarded as a special kind of authigenic component. Unlike carbonate, the organic matter generally contains high amounts of REEs along with many elements (i.e. U, V, and Mo, etc.)

This study evaluated shale rock samples from four prominent reservoirs from the United States including the Utica, Niobrara, Mancos, and Green River Formations. The shale samples characterized in this study were chosen for their diversity and rich hydrocarbon reservoirs. Furthermore, two of Ohio Well (Utica Formation) samples were chosen to highlight the vast diversity of mineralogical and inorganic compositions that can exist within the same shale formation.

The elemental composition and morphological properties of shale were evaluated in this study using spectroscopy, microscopic, and mass spectrometric techniques. To our knowledge, this is the first study to perform a complete dissolution of shale using a microwave-acid digestion used for bulk elemental analysis couple with microstructural and geochemical analysis. This dissolution enabled the complete quantification of inorganic metals present and the ability to relate shale's geochemistry to its diagenesis.

3.3 Materials and Methods

Figure 3.1 highlights the geologic setting of the shale formation used in this study. Shale solid rock samples of the Niobrara, Mancos, and Green River were acquired from the University of Utah Energy Geoscience Institute (EGI), whereas two samples taken at different depths from the Utica Formation, Ohio Well core samples seen in supplementary information, Figure 3.8, were acquired from the USGS. Shown in Figure 3.2 is a flowchart for the separation of aliquots used for analysis. Shale samples begin as solid rock pieces separated into aliquots and prepared for analysis. The initial samples were sub-sampled and prepared as polished thin sections and embedded in an epoxy 'puck' and carbon coated, using the method of Gottlieb et al. (2000) and Pirrie et al. (2004). Then solid rock pieces were crushed with a hammer and sifted through a 0.9 mm brass mesh sieve. The bench top surface, hammer, and the brass sieve were cleaned before and after sample with a 3% nitric acid solution and rinsed with ultrapure 18.2 MΩ water to prevent cross-transfer between samples. For verification of minimal or no cross-contamination between samples, swipes taken from the surface of the bench top, hammer, and brass sieve were analyzed on the iCAP Q ICP-MS (Thermo Scientific).

The microstructural characteristics of samples from each deposit were investigated using SEM/EDX and XRD. SEM/EDX analysis was performed on a Cameca SX-50 electron microprobe with four wavelength-dispersive spectrometers. Analytical conditions were 15 keV accelerating voltage, 25 nA beam current, and a nominal beam diameter of 10 μm, and a combination of natural and synthetic standards were employed. Raw X-ray intensities were corrected for matrix effects with a phi-rho-z algorithm (Pouchou, 1993). The nominal detection limit for these operating conditions is 0.03 wt %.

A whole-rock and clay XRD analysis was performed; each sample aliquot was placed on a glass holder and analyzed using a Panalytical X'Pert X-Ray Diffractometer. The diffractometer was operated on a Gonio scan axis from of 10^{o} to 90^{o} 2θ with a step of 0.02 and scan time of 0.5 seconds per step. Data were collected and analyzed using the X'Pert Data Collection program accompanied by inorganic crystal structure database (ICSD) for pattern analysis.

Bulk elemental analyses were performed using mineral acid digestions followed by ICP—MS analysis. A trace metals grade reagent was used for all the dissolution and separation experiments. The dissolution of the shale proved challenging, possibly due to high concentration of carbonates, silicates, and organics, known to cause difficulties in dissolution and creating participates, although silicates were most likely removed through the use of HF and evaporation (Galindo et al., 2007, Bhargava et al., 2015). This required a modification to the original procedure adapted from Snow et al. (2015). Figure 3.3 outlines the procedure used for shale dissolution; the first step was to dry the soil at 110^{o}C in a laboratory oven for 12 hours, then a triplicate 0.25 g aliquot of each shale sample was added to individual microwave-acid digestion vessel, along with 4 mL of concentrated nitric acid and 4 mL of concentrated hydrofluoric acid. The vessel was then immediately sealed and microwaved using a CEM MARS 5 microwave digestion system. After the microwave sequence, the vessels were removed and the samples were dried using hotplates, blocks, and heat lamps. Shale samples required a second microwave-acid digestion with 4 mL of concentrated nitric acid and 4 mL of concentrated hydrofluoric acid to acquire complete dissolution. The samples were then dried, cooled, then brought up in 5 mL of 22 g/L of boric acid for a third microwave digestion. Upon cooling, the

samples were quantitatively transferred with three 1 mL rinses of 2% nitric acid solution to 15 mL centrifuge tubes. The samples were then diluted, using 2% nitric acid at 1:10,000 times with the addition of a 1 ppb Germanium which served as the internal standard.

The concentration of the inorganic metals was determined using an iCAP Q ICP-MS (Thermo Scientific). Calibration of the instrument was performed using the QTEGRA computer program and Inorganic Ventures 4ARVE Tune B solution. Germanium (VHG Labs VHG-LGENF-100) was used as an internal standard and concentrations were determined by comparison to a matrix matched calibration curve generated by dilutions from High-Purity Multi-Element Standards ICP-MS-68B Solution A and B. Method blank samples (samples containing all reagents except soil/shale) routinely showed insignificant levels of contamination and elemental concentrations that were far below the samples elemental concentrations. Method validations were performed by via digestion/analysis of the NIST 2710a; bulk elemental analysis results from 2710a analyses were in quantitative agreement with the certified values validating the samples complete digestion and characterization (see supplementary information Table 3.3).

3.4 Results and Discussion

3.4.1 XRD Analysis

XRD spectral analysis results are shown in Table 3.1. Figure 3.4 shows an example of spectral analysis for the Mancos Shale Formation. The results show that the shales are mainly composed of quartz, feldspar (orthoclase and plagioclase, potash feldspar and

plagioclase), carbonates (calcite and dolomite), and clay minerals (illite, illite/smectite, ankerite, chlorite, and pyrite). The clay minerals content ranged from 4% to 39%, the quartz + feldspar contents ranged from 19.2% to 66.7%, and the dolomite + calcite contents ranged from 5% to 46%. The mineral composition of the shale was determined using XRD with results represented on a ternary diagram (Figure 3.5) to illustrate which samples fall within the ductile/brittle zone desired for hydraulic fracturing. Analysis to differentiate brittle from ductile rocks has been key to stimulation success in shale gas reservoirs, especially in shales where brittleness is mainly controlled by quartz content. High contents of brittle minerals make a reservoir highly brittle and easier to create network fractures and achieve volume reformation. The brittleness of shale is related to its mineralogy, and quartz has an important influence. Based on the mineralogy content, ductility is controlled by clay, calcite, and organic content.

XRD analysis shows differences in the mineral content of the two Utica shale samples, despite the fact that they are from the same formation and only separated by a few feet in sample depth. The quantitative evaluation of minerals by scanning electron microscopy (QEMSCAN®) analyses of the solid rock samples was completed on a QEMSCAN® 4300, which is built on a Zeiss Evo 50 SEM platform with four light element Bruker Xflash energy dispersive X-ray detectors. The initial samples were sub-sampled and prepared as polished thin sections and embedded in an epoxy 'puck' and carbon coated. QEMSCAN® analysis reveals similar results as XRD. The QEMSCAN® approach to petrological analyses was used to quickly and accurately characterize bulk mineralogy, fabrics/textures, and mineral associations. Colors of the image are related to the type of mineral, and each mineral can be quantified and related to its associated elemental make-

up. Supplementary information, Figure 3.9 and Figure 3.10 show a comparison of Utica formation taken at the depths of 33.58' and 31.5'. Utica 33.58' is predominantly comprised of dolomite, illite, and quartz. Utica 31.5' has a majority of illite and quartz, with a minimum amount of dolomite. However, with close inspection of the elemental analysis, the samples are similar and fit into the expectation for the Utica formation.

3.4.2 SEM/EDX Analysis

SEM/EDX was conducted on selected samples to evaluate the inorganic composition near dense hydrocarbon regions. Figure 3.6 shows the results from one Utica sample (31.5'). The correlation between sulfur (Figure 3.6C), iron (Figure 3.6F), molybdenum (Figure 3.6G), and titanium (Figure 3.6E) suggests the mineral signatures from pyrite (FeS_2) and iron-titanium oxides (Fe-Ti Oxides; magnetite, illite, and spinel) (Tribovillard et al., 2006, Chermak et al., 2014). Silicate minerals show up faintly on the Fe EDX image (Figure 3.6F) due to clays (i.e. illite) containing Fe (Tribovillard et al., 2006, Chermak et al., 2014).

The organic material has a relatively small amount of S present, while the Mo concentrations are high, potentially due to the capture of Mo by FeS_2 forming Mo-Fe-S cuboidal clusters of pyrite, which is consistent with an anoxic marine environment for the shale deposition (Tang et al., 2014, WoldeGabriel et al., 2014). The carbon abundance (Figure 3.6A) is low throughout the clay and quartz matrix of the sample and is high in the presence of the organic material (Tribovillard et al., 2008).

The U (Figure 3.6I) has a relatively lower concentration in the organic material and quartz and a higher concentration in the clay dominated-matrix of the rock. The higher

concentration of U in the clay dominated-matrix of the rock may indicate the migration of U from the main organic material within the rock.

3.4.3 Bulk Elemental Analyses

Rare earth elements (REEs) are often considered stable during weathering, erosion, transportation, deposition, and early diagenesis, enabling them effective in tracing the material source of sediments and revealing the provenance. The concentrations of these elements via bulk elemental analyses are shown in Figure 3.7 and supplemental information Table 3.4. As seen in Figure 3.7, the concentrations of the REEs for the five samples studied are considerably low. Hence, the total concentration of REE's (ΣREE) was used to reveal the possible source of REEs for these shale samples. As shown in Table 3.2, all shales are considered to have a low ΣREE when compared to the North American Stratigraphic Code (NASC) (Banner, 2004, Abanda et al., 2006, Lev et al., 2008, and Asai et al., 2015).

The low ΣREE in all shale samples of this work indicates a high sedimentation rate that had a minimum exposure time in the marine environment and the adsorption of REEs, as is often observed in shales, and are of terrigenous origin (Bai et al., 2015). Since most REEs possess similar atomic radii and oxidation states, REEs can substitute for each in various crystal lattices. This capability of substitution leads to multiple REE occurrences within a single mineral and has resulted in a wide distribution within the Earth's crust. REEs are found in a wide range of mineral types, including halides, carbonates, oxides, phosphates, and silicates. REEs exists in the trivalent state for most natural conditions, except cerium and europium that exhibit variations as a function of

oxidation-reduction conditions found in natural sedimentary or oceanic environments (Wilde et al., 1996). As mentioned early, among the REEs, Ce and Eu occur in multiple valence states in marine environments, and thus would be expected to partition differently into shale depending on the marine oxidation state. As a result, the positive Ce anomalies with the negative Eu anomalies suggest a prolonged sedimentation below redox chemocline in deep waters (Wilde et al., 1996). Data further suggest that REE enrichment is of terrigenous origins (Wilde et al., 1996).

In contrast to the REEs, U is relatively more abundant in the shales studied than are commonly observed in NASC. Uranium in shale is often found in a reduced form and in association with organic matter in low energy environments, i.e. conditions under which marine shales are deposited (McKelvey and Nelson, 1950). Trace element combination and the ratio of U/Th and authigenic uranium (U_a) can be used to indicate the redox conditions of sediments. Ratios of U/Th higher than 1.25 mark an anoxic environment, 0.75–1.25 a suboxic to dysoxic environment, and lower than 0.75 indicates an oxic environment (Bai et al., 2015). The U_a is an index of bottom water anoxia in ancient sedimentary sequences and is determined by equation 1:

$$U_a = U - \frac{Th}{3} \quad (1)$$

A U_a content higher than 12.0 indicates anoxic conditions and 5.0–12.0 indicates suboxic to dysoxic conditions, while the U_a content lower than 5.0 indicates oxic conditions (Bai et al., 2015). As shown by Table 3.1, the results for the U/Th ratios and U_a are in good agreement, indicating that Utica (31.58'), Utica (31.5'), and Niobrara were

formed in an anoxic environment. While the Green River formation U/Th ratio could be anoxic or oxic with variation in the error, via propagation, the U_a would indicate an oxic environment. U/Th and U_a both indicate an oxic depositional environment for the Mancos formation. Shale sediments rich in organic matter can contain high concentrations of U, through adsorption of U by organic matter (Lev and Filer, 2004, Banda and Hannigan, 2006, Yu et al., 2014). Polar organic molecules contained in humic acids, particularly short-chain aliphatic carboxylate ions, are known to be capable of complexing the more common rock-forming metals (WoldeGabriel et al., 2014). A higher concentration of uranium has been shown to be associated with the shale formations higher in carbonaceous material.

The low Mn concentration in the shales can indicate a dysoxic environment, because under reducing conditions at the sediment/water interface, soluble Mn^{2+} (insoluble Mn^{4+}) diffuses from the sediments into the oxygen-depleted waters (Landing and Bruland, 1980, Landing and Bruland, 1987, Bruland, 1991). Average concentrations of V, Cr, Ni, Zn, As, Y, Mo, Ba, Pb, and U in the shales formations are higher than those for typical shales and mudstones in the crust; this is consistent with the low energy environment for shale deposition (McLennan and Hemming, 1992, Nyakairu et al., 2001). The presence of Rhenium and Molybdenum also supports the low energy environment for shale depositional systems (Tribovillard et al., 2004).

Taking all the geochemical and mineralogical data together, we suggest that the anoxic conditions during deposition may have led to the enrichment of the redox-sensitive elements (i.e. U, V, and Mo, etc.) in the Utica and Niobrara formations, while an oxic depositional environment led to a depletion of redox-sensitive elements in the Green

River and Mancos formations. Our data suggest that the anoxic conditions created during the sediment layer formation led to the accumulation of uranium and other trace elements in the black shale. Mineralogical and elemental information about shale reservoirs could prove useful to address potential negative environmental impacts and assist with mitigation approaches of the expanding hydraulic fracturing used in hydrocarbon extraction.

3.5 References

(1) Abanda, P. A.; Hannigan, R. E. Effect of Diagenesis on Trace Element Partitioning in Shales. *Chem. Geol.* 2006, *230*, 42–59.

(2) Asai, S.; Limbeck, A. LA-ICP-MS of Rare Earth Elements Concentrated in Cation-Exchange Resin Particles for Origin Attribution of Uranium Ore Concentrate. *Talanta* 2015, *135*, 41–49.

(3) Badics, B.; Vető, I. Source Rocks and Petroleum Systems in the Hungarian Part of the Pannonian Basin: The Potential for Shale Gas and Shale Oil Plays. *Mar. Pet. Geol.* 2012, *31*, 53–69.

(4) Bai, Y.; Liu, Z.; Sun, P.; Liu, R.; Hu, X.; Zhao, H.; Xu, Y. Rare Earth and Major Element Geochemistry of Eocene Fine-Grained Sediments in Oil Shale- and Coal-Bearing Layers of the Meihe Basin, Northeast China. *J. Asian Earth Sci.* 2015, *97*, 89–101.

(5) Banner, J. L. Radiogenic Isotopes: Systematics and Applications to Earth Surface Processes and Chemical Stratigraphy. *Earth-Science Rev.* 2004, *65*, 141–194.

(6) Bernard, S.; Horsfield, B.; Schulz, H.-M.; Wirth, R.; Schreiber, A.; Sherwood, N. Geochemical Evolution of Organic-Rich Shales with Increasing Maturity: A STXM and TEM Study of the Posidonia Shale (Lower Toarcian, Northern Germany). *Mar. Pet. Geol.* 2012, *31*, 70–89.

(7) Bhargava, S. K.; Ram, R.; Pownceby, M.; Grocott, S.; Ring, B.; Tardio, J.; Jones, L. A Review of Acid Leaching of Uraninite. *Hydrometallurgy* 2015, *151*, 10–24.

(8) Bowell, R. J.; Grogan, J.; Hutton-Ashkenny, M.; Brough, C.; Penman, K.; Sapsford, D. J. Geometallurgy of Uranium Deposits. *Miner. Eng.* 2011, *24*, 1305–1313.

(9) Bruland, K. W.; Donat, J. R.; Hutchins, D. A. Interactive Influences of Bioactive Trace Metals on Biological Production in Oceanic Waters. *Limnol. Oceanogr.* 1991, *36*, 1555–1577.

(10) Chermak, J. a.; Schreiber, M. E. Mineralogy and Trace Element Geochemistry of Gas Shales in the United States: Environmental Implications. *Int. J. Coal Geol.* 2014, *126*, 32–44.

(11) Clarkson, C. R. Production Data Analysis of Unconventional Gas Wells: Review of Theory and Best Practices. *Int. J. Coal Geol.* 2013, *109-110*, 101–146.

(12) Galindo, C.; Mougin, L.; Nourreddine, A. An Improved Radiochemical Separation of Uranium and Thorium in Environmental Samples Involving Peroxide Fusion. *Appl Radiat Isot* 2007, *65*, 9–16.

(13) Haque, N.; Norgate, T. The Greenhouse Gas Footprint of in-Situ Leaching of Uranium, Gold and Copper in Australia. *J. Clean. Prod.* 2014, *84*, 382–390.

(14) Landa, E. R. Uranium Mill Tailings: Nuclear Waste and Natural Laboratory for Geochemical and Radioecological Investigations. *J. Environ. Radioact.* 2004, *77*, 1–27.

(15) Lev, S. M.; Filer, J. K.; Tomascak, P. Orogenesis vs. Diagenesis: Can We Use Organic-Rich Shales to Interpret the Tectonic Evolution of a Depositional Basin? *Earth-Science Rev.* 2008, *86*, 1–14.

(16) McGlade, C.; Speirs, J.; Sorrell, S. Unconventional Gas – A Review of Regional and Global Resource Estimates. *Energy* 2013, *55*, 571–584.

(17) McLennan, S. M.; Hemming, S. Samarium / Neodymium Elemental and Isotopic Systematics in Sedimentary Rocks. *Geochim. Cosmochim. Acta* 1992, *56*, 887–898.

(18) Nyakairu, G. W. a.; Koeberl, C. Mineralogical and Chemical Composition and Distribution of Rare Earth Elements in Clay-Rich Sediments from Central Uganda. *Geochem. J.* 2001, *35*, 13–28.

(19) Pouchou, J. L. X-Ray Microanalysis of Stratified Specimens. *Anal. Chim. Acta* 1993, *283*, 81–97.

(20) Rivard, C.; Lavoie, D.; Lefebvre, R.; Séjourné, S.; Lamontagne, C.; Duchesne, M. An Overview of Canadian Shale Gas Production and Environmental Concerns. *Int. J. Coal Geol.* 2014, *126*, 64–76.

(21) Sachsenhofer, R. F.; Koltun, Y. V. Black Shales in Ukraine – A Review. *Mar. Pet. Geol.* 2012, *31*, 125–136.

(22) Selley, R. C. UK Shale Gas: The Story so Far. *Mar. Pet. Geol.* 2012, *31*, 100–109.

(23) Skalak, K. J.; Engle, M. a.; Rowan, E. L.; Jolly, G. D.; Conko, K. M.; Benthem, A. J.; Kraemer, T. F. Surface Disposal of Produced Waters in Western and Southwestern Pennsylvania: Potential for Accumulation of Alkali-Earth Elements in Sediments. *Int. J. Coal Geol.* 2014, *126*, 162–170.

(24) Snow, M. S.; Snyder, D. C.; Mann, N. R.; White, B. M. Method for Ultra-Trace Cesium Isotope Ratio Measurements from Environmental Samples Using Thermal Ionization Mass Spectrometry. *Int. J. Mass Spectrom.* 2015, *381-382*, 17–24.

(25) Sovacool, B. K. Cornucopia or Curse? Reviewing the Costs and Benefits of Shale Gas Hydraulic Fracturing (fracking). *Renew. Sustain. Energy Rev.* 2014, *37*, 249–

264.

(26) Tang, X.; Zhang, J.; Wang, X.; Yu, B.; Ding, W.; Xiong, J.; Yang, Y.; Wang, L.; Yang, C. Shale Characteristics in the Southeastern Ordos Basin, China: Implications for Hydrocarbon Accumulation Conditions and the Potential of Continental Shales. *Int. J. Coal Geol.* 2014, *128-129*, 32–46.

(27) Tribovillard, N.; Algeo, T. J.; Lyons, T.; Riboulleau, A. Trace Metals as Paleoredox and Paleoproductivity Proxies: An Update. *Chem. Geol.* 2006, *232*, 12–32.

(28) Wang, G.; Ju, Y.; Han, K. Early Paleozoic Shale Properties and Gas Potential Evaluation in Xiuwu Basin, Western Lower Yangtze Platform. *J. Nat. Gas Sci. Eng.* 2015, *22*, 489–497.

(29) Wang, Q.; Chen, X.; Jha, A. N.; Rogers, H. Natural Gas from Shale Formation – The Evolution, Evidences and Challenges of Shale Gas Revolution in United States. *Renew. Sustain. Energy Rev.* 2014, *30*, 1–28.

(30) Weijermars, R.; Drijkoningen, G.; Heimovaara, T. J.; Rudolph, E. S. J.; Weltje, G. J.; Wolf, K. H. a. a. Unconventional Gas Research Initiative for Clean Energy Transition in Europe. *J. Nat. Gas Sci. Eng.* 2011, *3*, 402–412.

(31) Wilde, P.; Quinby-Hunt, M. S.; Erdtmann, B.-D. The Whole-Rock Cerium Anomaly: A Potential Indicator of Eustatic Sea-Level Changes in Shales of the Anoxic Facies. *Sediment. Geol.* 1996, *101*, 43–53.

(32) WoldeGabriel, G.; Boukhalfa, H.; Ware, S. D.; Cheshire, M.; Reimus, P.; Heikoop, J.; Conradson, S. D.; Batuk, O.; Havrilla, G.; House, B.; et al. Characterization of Cores from an in-Situ Recovery Mined Uranium Deposit in Wyoming: Implications for Post-Mining Restoration. *Chem. Geol.* 2014, *390*, 32–45.

(33) Landing, W. M.; Bruland, K. W. Manganese-in-the-North-Pacific_1980_Earth-and-Planetary-Science-Letters. *Geochim. Cosmochim. Acta* 1980.

(34) Bruland, K. W.; Franks, R. P.; Landing, W. M. Southern-California-Inner-Basin-Sediment-Trap-calibration_1981_Earth-and-Planetary-Science-Letters. *Earth Planet. Sci. Lett.* 1980.

(35) Landing, W. M.; Bruland, K. W. The-Contrasting-Biogeochemistry-of-Iron-and-Manganese-in-the-Pacific-Ocean_1987_Geochimica-et-Cosmochimica-Acta. *Earth Planet. Sci. Lett.* 1980.

(36) McKelvey, V. E., and Nelson, J. M. Characteristics of Marine Uranium-Bearing Sedimentary Rocks. *Econ. Geol.* 1950, *45*, 35–53.

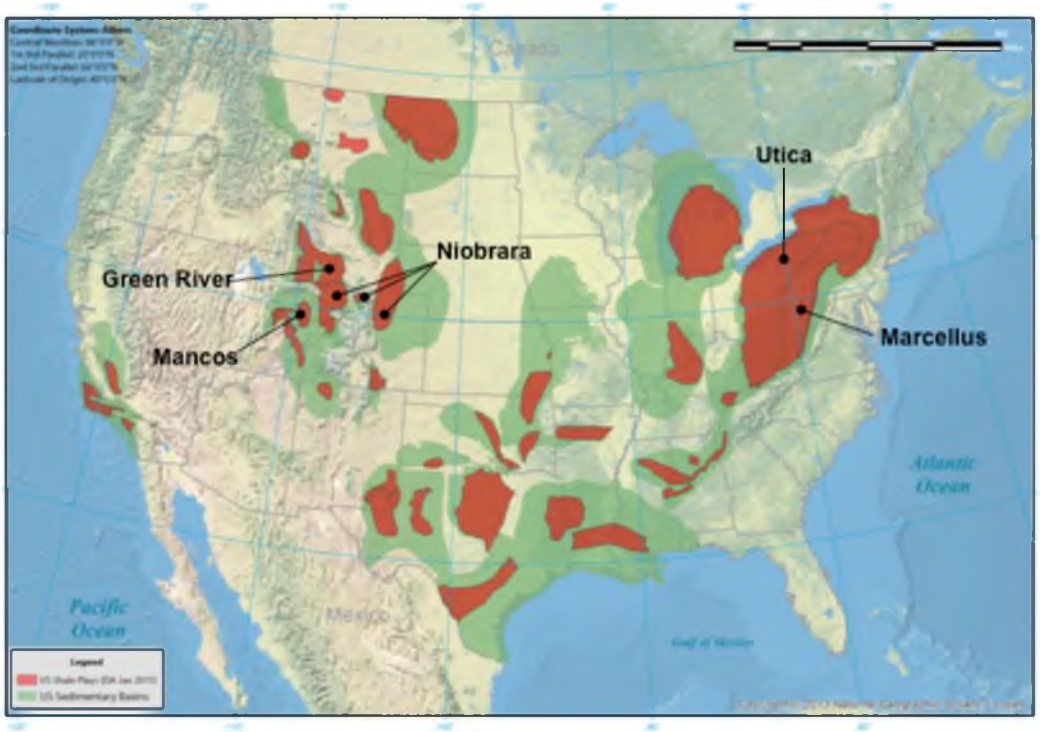

Figure 3.1 U.S. Shale Plays. U.S. Shale plays showing the geologic setting for the samples used in this study; Mancos, Marcellus, Niobrara, Green River and two Utica samples from the Ohio Well. (Image adapted from 2013 National Geographic Society)

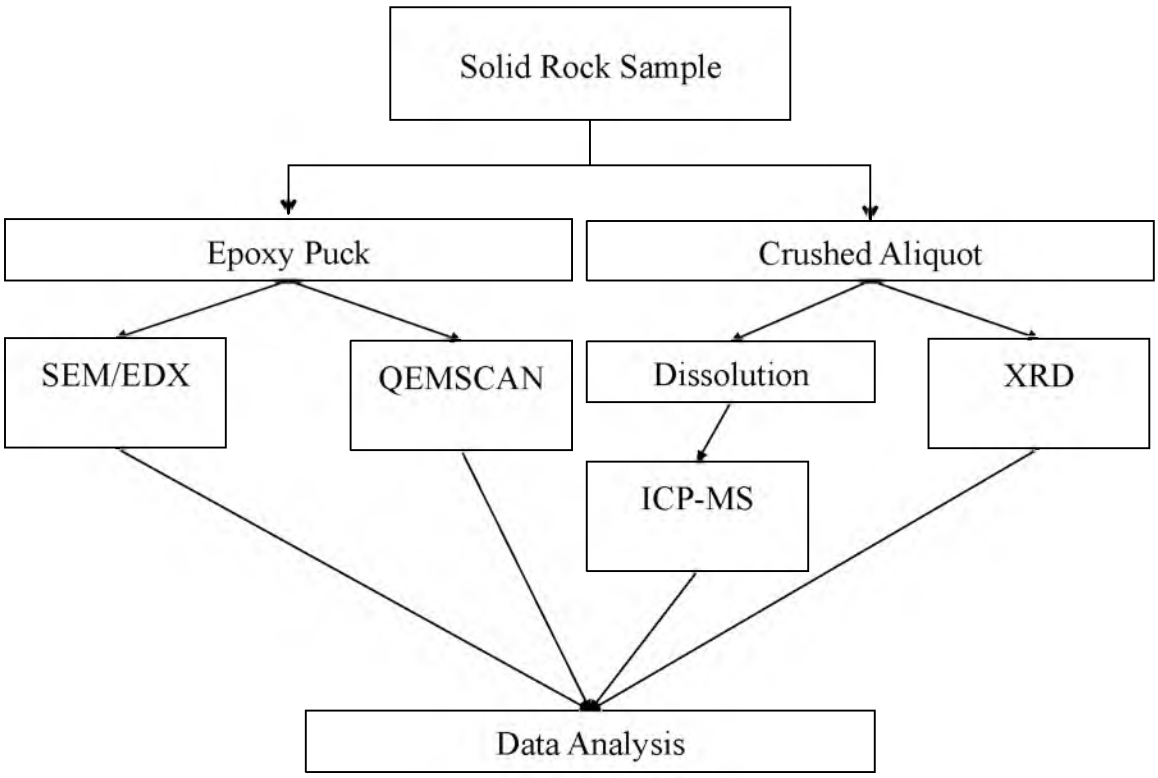

Figure 3.2 Sample Preparation Flowchart. Flowchart for the separation of aliquots used for analysis.

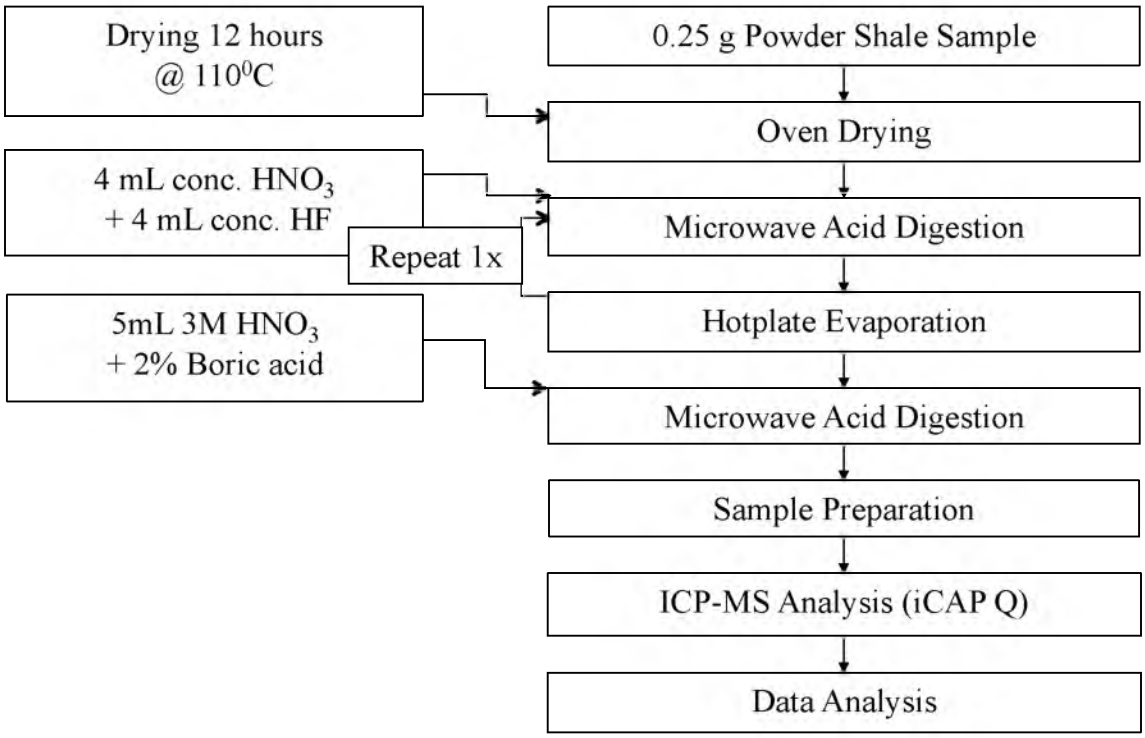

Figure 3.3 Dissolution Flowchart. Flowchart outlining the shale dissolution procedure, and analysis process.

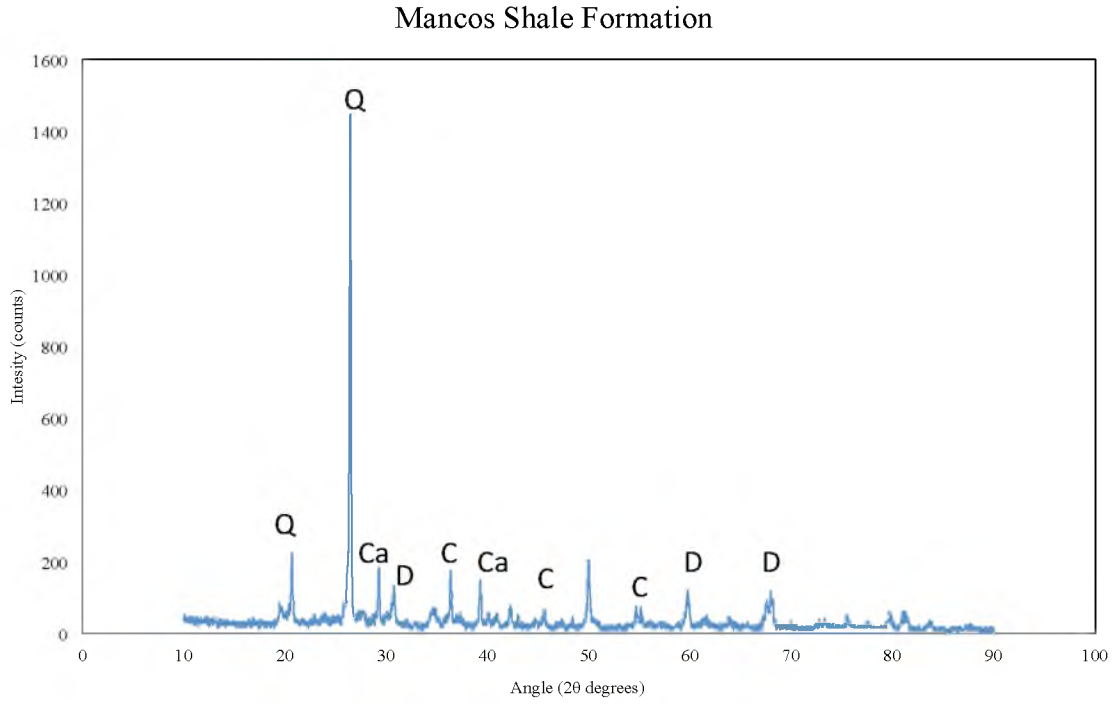

Figure 3.4 XRD analysis. Identification of various mineral phases in the Mancos shale formation, under XRD analysis. Explanations: C: clays; Q: quartz; D: dolomite; Ca: calcite.

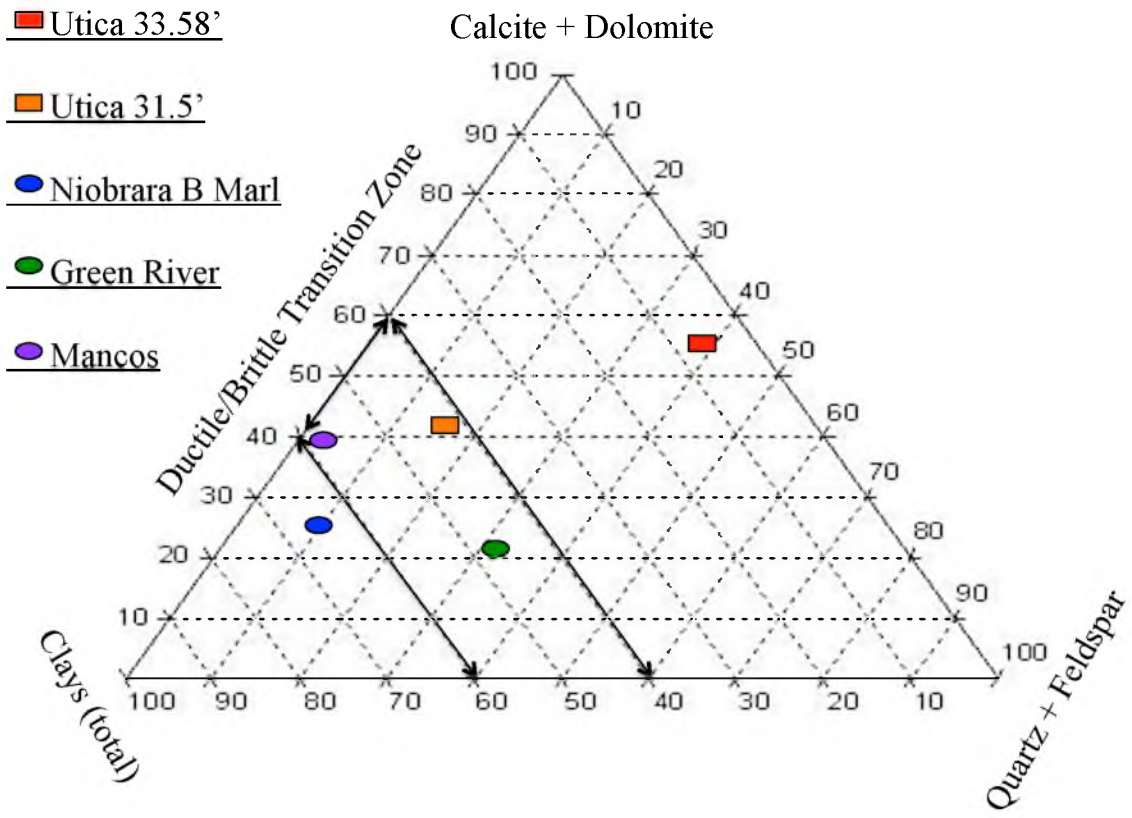

Figure 3.5 XRD Ternary Diagram. Ternary diagram from the XRD analysis of shale formations evaluated in this study. Samples within the ductile brittle transition zone are predominantly used for gas and/-or oil production, while samples above the ductile brittle transition zone do not have enough organic matter to produce a reliable production zone and shale samples below the ductile brittle transition zone make for difficult extraction of oil and/-or gas.

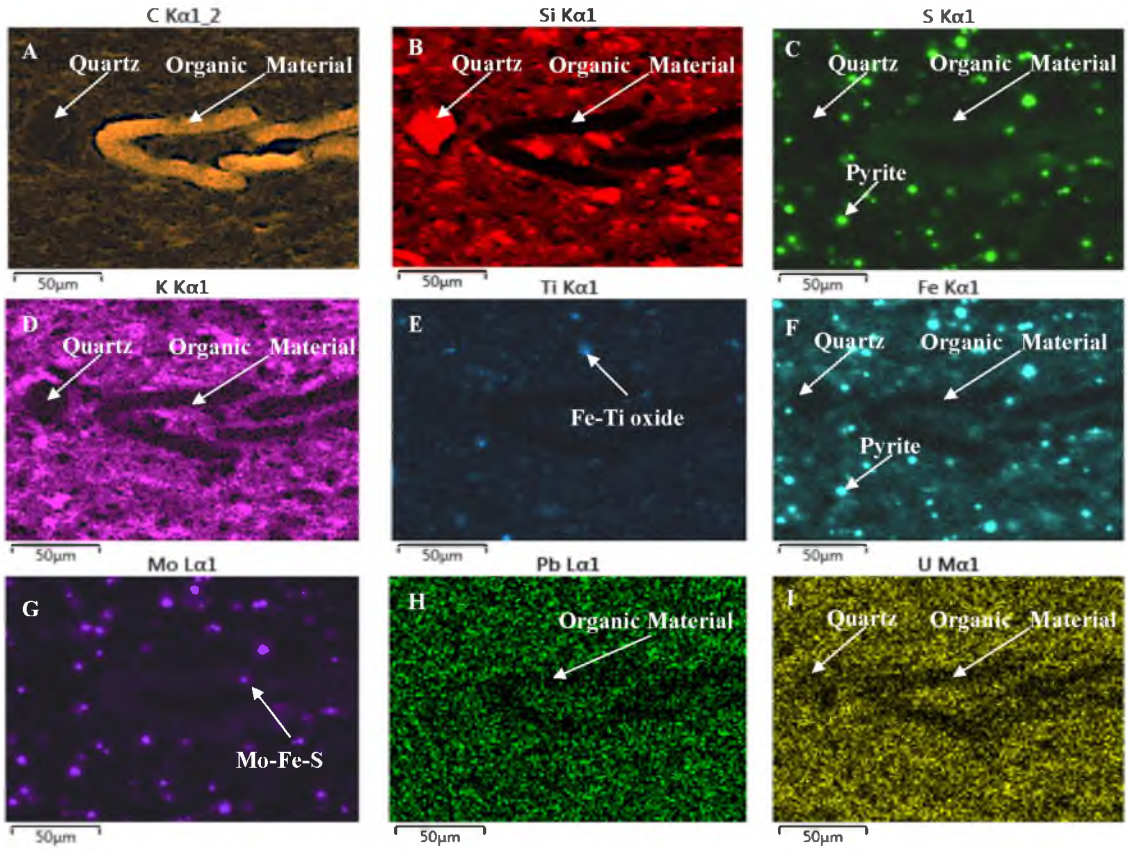

Figure 3.6 SEM/EDX Analysis of Utica Sample. SEM/EDX analysis of the Utica sample (31.5') carbon (A), silicone (B), sulfur (C), potassium (D), titanium (E), iron (F), molybdenum (G), lead (Pb), and uranium (I). The high-density concentration of carbon helps reveal the organic material region while the similarities in the concentration of Fe and S helps reveal pyrite rich regions. The concentration of U and Pb follow a similar trend, indicating that most Pb is present as a decay species of U. Both have a relatively lower concentration in the organic material then the surrounding area.

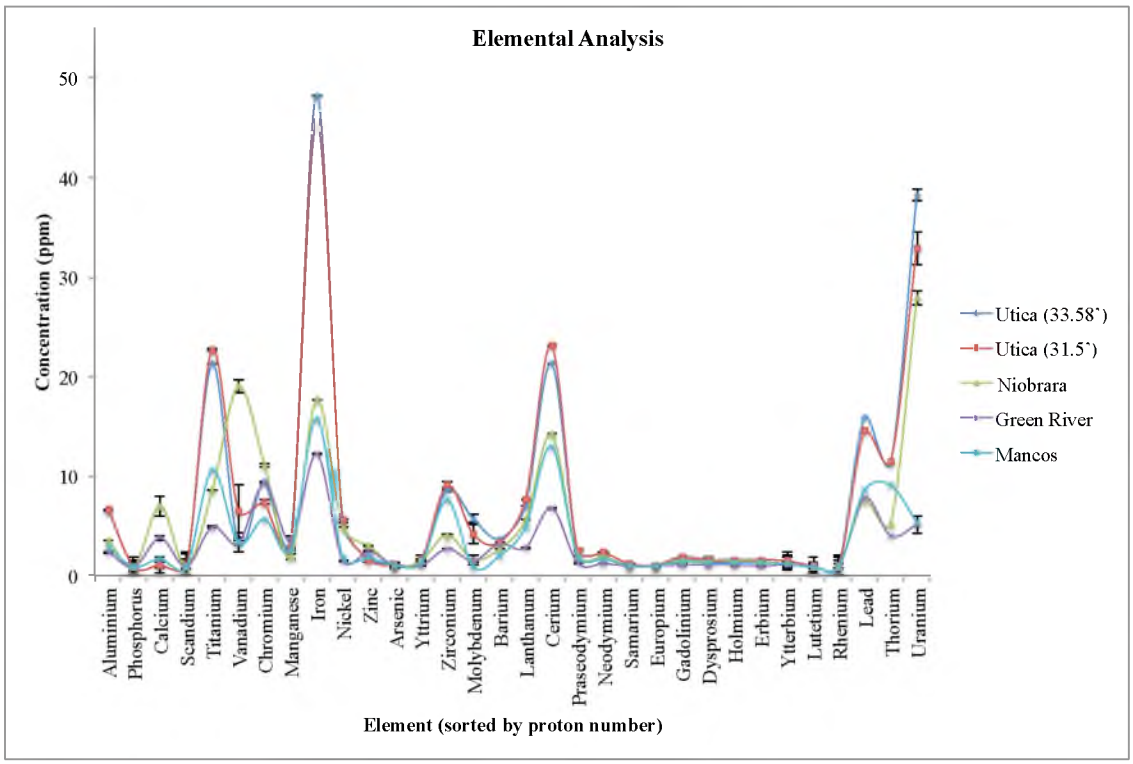

Figure 3.7 ICP-MS Analysis of Shale Samples. ICP/MS analysis of various metals in the shale samples. The concentration of rare earth elements is relatively low in all shale samples The Utica formation and Niobrara has a high concentration of U.

Table 3.1 XRD Analysis

Shale	Quartz + feldspar (Silicate) (%)	Calcite + Dolomite (Carbonate) (%)	Clay (%)
Mancos	66.7	29.3	4
Green River	19.2	39.3	27.2
Niobrara	45	46	9
Utica 31.5'	56	5	39
Utica 33.58'	55	22	19

Table 3.2 Trace Elements, U/TH Ratio, and Authigenic Uranium. Trace element combination and the ratio of U/Th and authigenic uranium (U_a).

Shale Formation	U/Th	U_a (ppb)	ΣREE (ppb)
Utica (33.58')	3.35 ± 1	34.4 ± 0.13	44.6 ± 0.55
Utica (31.5')	2.86 ± 1.5	29.1 ± 0.93	46.9 ± 1.68
Niobrara	5.37 ± 1.8	26.2 ± 0.73	33.6 ± 0.72
Green River	1.28 ± 3	3.8 ± 0.53	20.4 ± 0.86
Mancos	0.59 ± 1.33	2.4 ± 0.3	30.9 ± 0.94

3.6 Supplementary Information

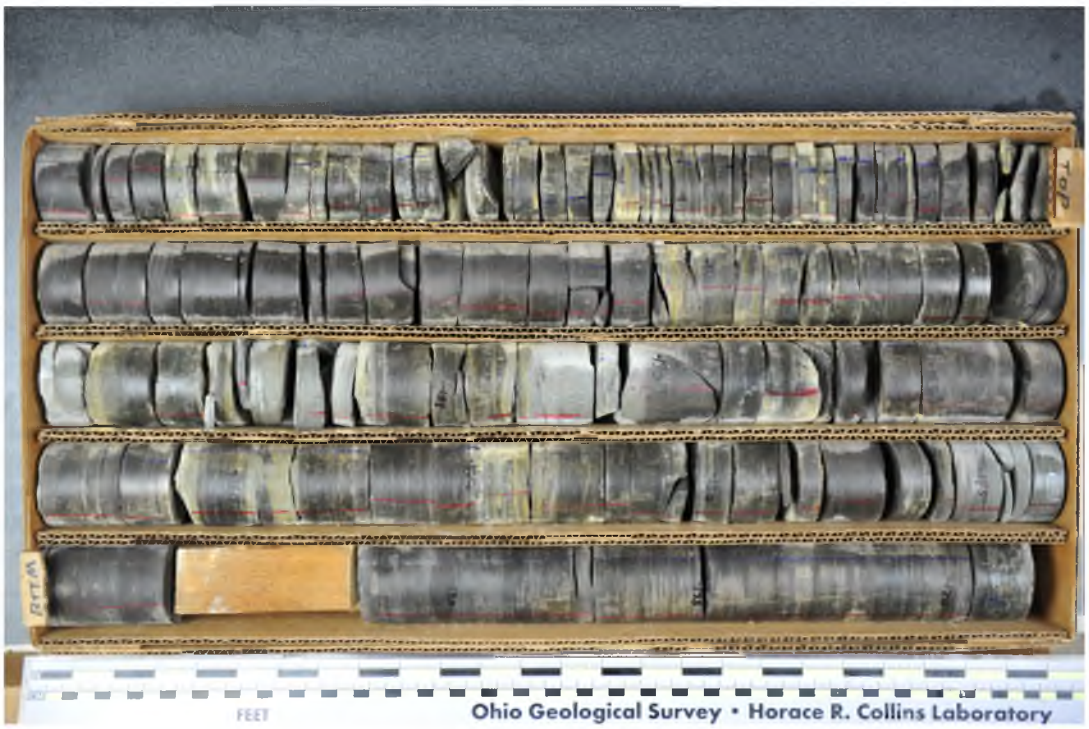

Figure 3.8 Ohio Well Core Samples. Utica Formation core samples provided by the USGS.

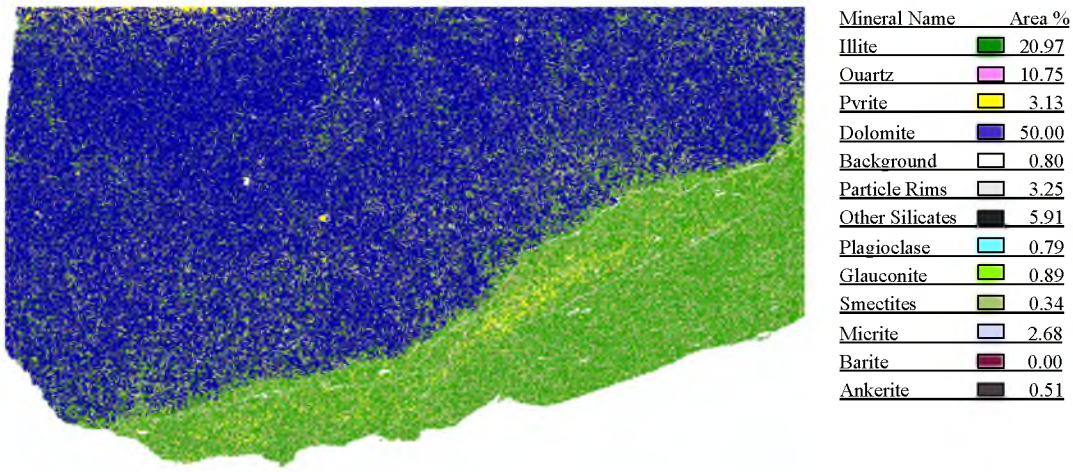

Figure 3.9 Utica Formation 33.58'. Paleozoic Era, Ordovician Period (460 Ma)

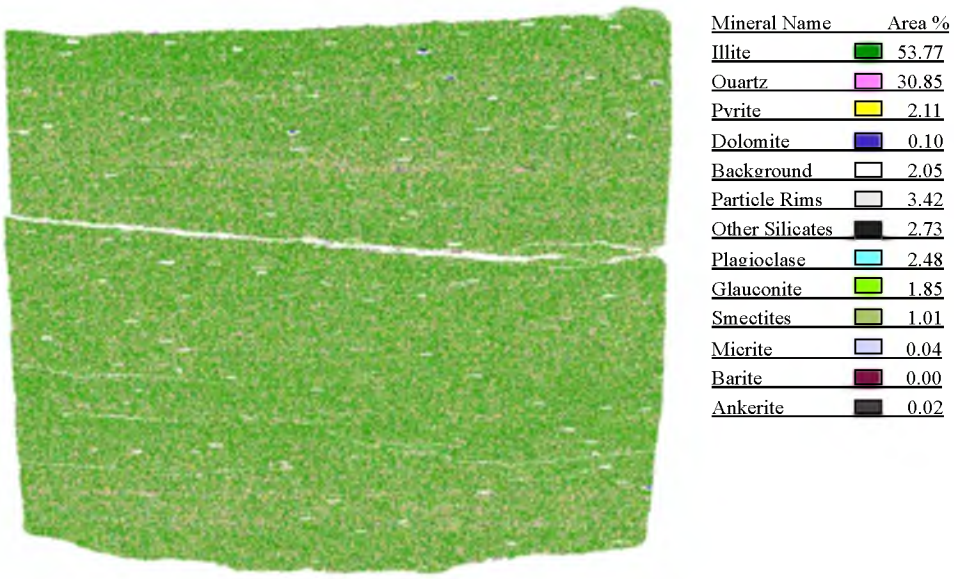

Figure 3.10 Utica Formation 31.50'. Paleozoic Era, Ordovician Period (460 Ma)

Table 3.3 Digestion Method Validation.

Method Validation	Uranium Concentration (ppm)
iCAP Q ICP-MS Data	9.14 ± 0.6
NIST Reported Value	9.11 ± 0.3

Table 3.4 ICP—MS Analysis. Analysis performed after dissolution of shale samples.

Shale Formation	**Utica (33.58')**	**Utica (31.5')**	**Niobrara**	**Green River**	**Mancos**
Element	**Elemental Concentration (ppm)**				
Aluminium	6.5 ± 0.1	6.6 ± 0.3	3.5 ± 0.1	2.3 ± 0.1	2.8 ± 0.2
Phosphorus	0.9± 0.0	0.9 ± 0.0	0.9 ± 0.0	0.9**± 0.1**	0.9± 0.1
Calcium	1.1 ± 0.0	1.1± 0.0	7± 0.4	3.8± 0.1	1.7± 0.1
Scandium	1.0 ± 0.02	1.0 ± 0.03	0.9 ± 0.01	0.9 ± 0.06	0.9 ± 0.06
Titanium	21.3 ±0.7	22.7 ± 0.9	8.6 ± 0.9	4.9 ± 0.4	10.6 ± 0.7
Vanadium	3.3 ± 0.3	6.5 ± 0.8	19.0 ± 1.0	3.3 ± 0.3	3.3 ± 0.4
Chromium	9.4 ± 1.17	7.4 ± 0.34	11.1 ± 0.85	9.3 ± 1.49	5.7 ± 0.13
Manganese	3.3 ± 0.02	2.7 ± 0.08	1.9 ± 0.05	3.5 ± 0.06	2.6 ± 0.09
Iron	48.2 ± 1.0	45.6 ±2.7	17.7 ± 0.7	12.2 ± 0.2	15.8 ± 0.3
Nickel	5.3 ± 0.06	5.7 ± 0.19	4.9 ± 0.18	1.5 ± 0.07	1.8 ± 0.6
Zinc	1.8 ± 0.4	1.6 ± 0.1	3.0 ± 0.3	2.4 ± 0.6	1.8 ± 0.2
Arsenic	1.1 ± 0.06	1.1 ± 0.08	1.0 ± 0.03	1.0 ± 0.07	1.1 ± 0.08
Yttrium	1.7 ± 0.03	1.6 ± 0.01	1.5 ± 0.02	1.0 ± 0.06	1.3 ± 0.07
Zirconium	8.6 ± 0.0	9.1 ± 0.3	4.1± 0.1	2.7± 0.1	7.6± 1.0
Molybdenum	5.70 ± 0.2	4.18 ± 0.2	1.6 ± 0.1	1.5 ± 0.1	0.9 ±0.2
Barium	3.7 ± 0.32	3.3 ± 0.9	2.7± 0.05	3.2± 0.04	2.0 ± 0.09

Table 3.4 Continued.

Shale Formation	**Utica (33.58')**	**Utica (31.5')**	**Niobrara**	**Green River**	**Mancos**
Element	**Elemental Concentration (ppm)**				
Lanthanum	7.0 ± 0.07	7.6 ± 3.3	5.6 ± 0.14	2.8 ± 0.07	4.9 ± 0.07
Cerium	21.3 ± 0.39	23.1 ± 0.93	14.2 ± 0.48	6.8 ± 0.11	13.0 ± 0.18
Praseodymium	2.5 ± 0.0	2.6± 0.1	2 ± 0.0	1.3± 0.1	1.9± 0.
Neodymium	2.3 ± 0.0	2.3 ± 0.0	1.9 ± 0.0	1.2 ± 0.1	1.7 ± 0.1
Samarium	1.2 ± 0.0	1.2 ± 0.0	1.0 ± 0.0	1.0 ± 0.1	1.0 ± 0.1
Europium	1.1 ±0.01	1.1 ± 0.03	1.0 ± 0.02	1.0 ± 0.06	1.0 ± 0.06
Gadolinium	1.9 ± 0.2	1.8 ± 0.2	1.6 ± 0.01	1.1 ± 0.06	1.4 ± 0.07
Dysprosium	1.6 ± 0.02	1.6 ± 0.01	1.4 ± 0.02	1.1 ± 0.07	1.3± 0.07
Holmium	1.6 ± 0.01	1.5 ± 0.01	1.4 ± 0.02	1.1 ± 0.06	1.3 ± 0.07
Erbium	1.6 ± 0.02	1.6 ± 0.02	1.4 ± 0.02	1.0 ± 0.07	1.3 ± 0.06
Ytterbium	1.5 ± 0.0	1.5 ± 0.2	1.2 ± 0.0	1.1 ± 0.0	1.2 ±0.0
Lutetium	1.0 ± 0.01	1.0 ± 0.03	0.9 ± 0.01	0.9 ± 0.06	0.9 ± 0.06
Rhenium	1 ± 0.0	0.9 ± 0.0	0.9 ± 0.0	0.9 ± 0.1	0.9 ± 0.1
Lead	15.9 ± 0.6	14.5 ± 0.9	7.6 ± 0.6	7.8 ± 0.3	8.6 ± 0.2
Thorium	11.4 ± 0.2	11.5 ± 0.8	5.2 ± 0.5	4.0 ± 0.2	9.1 ± 0.3
Uranium	38.2 ± 0.2	32.7 ± 1.1	27.9 ± 0.8	5.0 ± 0.1	5.4 ± 0.1

CHAPTER 4

CONCLUSION

The mineralogical and inorganic composition of various hydrocarbon rich shales was evaluated. Information gained provided significant insight into the sedimentological and burial diagenetic process of the host shales. Understanding element concentrations in shales has allowed for the interpretation of paleoenvironmental conditions during shale deposition. These elements, used as paleoredox indicators, arise from the geochemical behavior that different oxidation states of the elements exhibit under oxic, suboxic, and anoxic conditions. The main mineral phases implicated in the retention of trace elements are calcite, dolomite, quartz, and clays. Accessory minerals consist of pyrite, apatite, anhydrite, and feldspars. The NORM was associated predominantly with humic acids, the precursors of kerogen. Our data suggest that the anoxic conditions created during the sediment layer formation led to the accumulation of uranium and other trace elements in the black shale. Shale sediments rich in organic matter can contain high concentrations of U, through adsorption of U by organic matter (Lev and Filer, 2004, Abanda and Hannigan, 2006, Yu et al., 2014). Polar organic molecules contained in humic acids, particularly short-chain aliphatic carboxylate ions, are known to be capable of complexing the more common rock-forming metals (WoldeGabriel et al., 2014). A higher

concentration of uranium has been shown to be associated with the shale formations higher in carbonaceous material. REEs in the shale are of terrigenous origins indicated by both the total REEs and Ce concentrations.

Mineralogical and elemental information about shale reservoirs could prove useful to address potential negative environmental impacts and assist with mitigation approaches of the expanding hydraulic fracturing used in hydrocarbon extraction. In addition, an increase of nuclear power has resulted in a large demand for high-grade uranium ores. Generally, the uranium in these ores is extracted through a dynamic treatment where the rock is crushed and mechanically ground prior to extraction with organic solutions, ion exchange, or acid leaching. As observed in this study and as reported by the U.S. Geological survey, black shale in the U.S. has relatively high concentrations of uranium. For example, the Marcellus Shale, which extends through much of the Appalachian Basin, has uranium content of 8.9 – 83.7 ppm depending on the depth and geographical location. Understanding the chemical make-up of the uranium in these shales could enable these shale formations to be used as a source rock for uranium, not just hydrocarbons.

4.1 References

(1) Abanda, P. A.; Hannigan, R. E. Effect of Diagenesis on Trace Element Partitioning in Shales. *Chem. Geol.* 2006, *230*, 42–59.

(2) Lev, S. M.; Filer, J. K. Assessing the Impact of Black Shale Processes on REE and the U-Pb Isotope System in the Southern Appalachian Basin. *Chem. Geol.* 2004, *206*, 393–406.

(3) WoldeGabriel, G.; Boukhalfa, H.; Ware, S. D.; Cheshire, M.; Reimus, P.; Heikoop, J.; Conradson, S. D.; Batuk, O.; Havrilla, G.; House, B.; et al. Characterization of Cores from an in-Situ Recovery Mined Uranium Deposit in Wyoming: Implications for Post-Mining Restoration. *Chem. Geol.* 2014, *390*, 32–45.

(4) Yu, C.; Lavergren, U.; Peltola, P.; Drake, H.; Bergbäck, B.; Åström, M. E. Retention and Transport of Arsenic, Uranium and Nickel in a Black Shale Setting Revealed by a Long-Term Humidity Cell Test and Sequential Chemical Extractions. *Chem. Geol.* 2014, *363*, 134–144.